Tomás Sousa Lopes

Bachelor in Micro and Nanotechnologies Engineering

Dissertation for obtaining the degree of Master of Science in
Micro and Nanotechnology Engineering

Metal layer for enhancing optical reflection in passivation layers in thin film solar cells

Supervisor: Doctor Pedro Salomé, Group Leader, International Iberian Nanotechnology Laboratory

Co-Supervisor: Doctor Manuel J. Mendes, Post Doc Fellow, Faculty of Sciences and Technology, New University Of Lisbon

Examination Commitee:

Chairperson: Dr. Prof Rodrigo Martins

Rapporteurs: Dr. Prof. Pedro Salomé
Dr. Prof. José de Brito Correia

FACULDADE DE CIÊNCIAS E TECNOLOGIA
UNIVERSIDADE NOVA DE LISBOA

September,2018

*"*Blood, sweat and tears*"*
Bernardinho

Acknowledgments

This master thesis marks the end of my 5 year journey. As such I, in this section would like to acknowledge who help trough this journey. As such a big thank you to all.

Primeiramente, quero agradecer ao Prof. Dr. Rodrigo Martins e à Prof. Dr. Elvira Fortunato pela oportunidade de poder estudar neste curso, bem como de utilizar as instalações do CENIMAT e CEMOP durante a minha estadia. Um especial obrigado ao professor Hugo Águas, por ter informado da oportunidade de realizar esta tese de mestrado no INL.

Ao meu orientador, Prof. Dr. Pedro Salomé, por me ter recebido de braços abertos no seu grupo de investigação, durante este período. Não há palavras para agradecer todo o apoio que me forneceu durante a minha estadia no INL. Estou extremamente agradecido, por todas as discussões de resultados, os seus ensinamentos, a disponibilidade e o esforço que fez para arranjar tempo para as minhas dúvidas. Por tudo isto um grande obrigado!

Um especial obrigado ao Dr. Paulo Fernandes, por toda a sua boa disponibilidade, a sua transmissão de conhecimento, bem como pela ajuda e discussões que me ajudou a melhorar o meu manuscrito.

Um obrigado ao meu orientado na FCT, o Prof. Dr. Manuel Mendes, que me acolheu durante uma semana e pela sua grande ajuda nas simulações e pelas suas respostas as minhas questões durante o período da tese. Grande obrigado.

Ao Miguel Cunha, um grande agradecimento por toda a ajuda que me forneceu durante estes meses. Por toda a sua disponibilidade para as minhas dúvidas, os dias passados na sala limpa, por todo o apoio que me deu durante estes seis meses, bem como o tempo que teve a rever o manuscrito, um grande obrigado!

To Sourav Bose, for all the help and guidance during our cleanroom work, the teachings he gave me as well as for his big counsel on to write my thesis with “my eyes closed”. I hope that someday you will start drinking coffee again.

Para as outras pessoas que estiveram comigo no grupo ao longo destes meses. Ao Barbosa, por toda a sua ajuda na sala limpa, comentários para o manuscrito e também para todos os cafés que me tirou para me focar na escrita. Ao Ricardo, pela sua ajuda no inicio quando cheguei a braga e pelos dias em que ficávamos os dois até tarde no INL. Á Beatriz, pela sua boa disposição que contagiou o grupo todo, pelas suas sugestões de organização e também pelos amendoins que providenciou. Ao André e para a Célia que pelos os seus comentários perspicazes que ajudaram a melhor o manuscrito.

To INL staff that helped during my work. A big thanks to Jerome for being 100% available to us and for the e-beam exposures, to José for his availability and his help during the deposition and to Mariam for all the help she gave me, a big thank you.

A special thanks to Sirazul, Manuel Chapa and Miguel Alexandre, for all the help they gave me for the optical simulations.

Á minha outra família: os Grossos. Ricardo, Pera, Breno, Catela, André, Miguel, Opinião, Paulo, William, Raul, Gonçalo, Campoa. Obrigado por tornarem estes 5 anos, os melhores da minha vida. Todas as festas, jantares e momentos passados juntos irão estar para sempre comigo. É verdade em os amigos da faculdade são para a vida e eu tenho a certeza que vos levo para vida toda! Tambem não podia deixar de agradecer à Catarina e à Maria, por sempre estarem lá e por todos os momentos que passamos nestes 5 anos.

Um agradecimento ao Filipe Peixoto, o meu padrinho. Por todos os momentos passados, os chás ás 2 da manhã, as viagens para a cidade Universitária para os jogos bem como todas as festas, um grande obrigado!

Aos meus pais e irmãos, que sem eles esta aventura não seria possível! Por todo o seu apoio e carinho que me deram, especialmente nestes meses que passei em Braga. Já está quase a acabar, Mãe e Pai!

Por último, o meu grande agradecimento, à Daniela. Por todo o amor e apoio prestados durante esta caminhada, as nossas chamadas diárias por Face-Time para atenuar as saudades, sem isso, tudo se tornava mais difícil.

Abstract

Thin film, CIGS solar cells were able to achieve efficiency values higher than multicristalline silicon solar cells (22.9 % vs 22.3 %). However, a possible In scarcity, may increase its production costs, hence decreasing the CIGS thickness is of upmost importance for the technology to stay cost-competitive. However, when decreasing the CIGS thickness two main efficiency limitations arise; rear contact recombination and optical losses due to incomplete light absorption. The main focus of this thesis is to increase the rear optical reflection of an ultrathin CIGS solar cell. For that, six different metals (Ag, Au, Cu, Ta, Ti and Zn) and two metallic alloys (AlSiCu and TiW) were tested as possible candidates for increasing the rear optical reflection and a nanopattern point structure was employed with Al_2O_3 as the passivation layer. Optical simulations were conducted to verify which metals gives the highest enhancement at increasing the light absorption in the CIGS layer. The solar cells fabricated were heavily affected by the reaction of the metal layer with the CIGS. As such, an alternative solar cell architecture was developed to prevent such reaction by depositing a Mo layer to cover the point contacts. In the end, the solar cell that incorporate a TiW layer, managed to achieve a 3.69 % (absolute) enhancement in efficiency values over the reference solar cell.

Keywords: CIGS, metallic layer,rear reflection, optical simulation, TiW,

---

Resumo

Células solares de filme fino CIGS, conseguiram valores de conversão de energia superiores aos conseguidos por células solares de silício multicristalino (22.9 % vs 22.3%). Contudo, uma possível escassez de In pode levar a um aumento de custos de produção, consequentemente, uma redução de espessura da camada CIGS é altamente importante, para a tecnologia manter-se competitiva em termos de custo de produção. Contudo, ao reduzir a espessura do CIGS, dois problemas, que limitam a conversão de energia, surgem: a recombinação nas interfaces e a incompleta absorção de luz. O grande foco desta tese é de aumentar a reflecção optica traseira de uma célula solar ultrafina CIGS. Para tal, seis metais (Ag, Au, Cu, Ta, Ti e Zn) e duas ligas metálicas (AlSiCu e TiW) foram testados como possível candidatos, uma estrutura nano-padronizada com pontos de contacto foi utilizada e Al_2O_3 foi utilizado como camada de passivação. Simulações óticas, foram realizadas para averiguar qual metal dá o maior aumento na absorção de luz no CIGS. As células solares fabricadas, foram altamente afetadas pela reação da camada metálica com o CIGS e Se. Uma nova estrutura foi desenvolvida para prevenir tal reação ao depositar uma camada de Mo para cobrir os pontos de contacto. No final, a célula solar que incorpora TiW conseguiu um aumento (absoluto) de 3.69 % em conversão de energia sobre a célula solar de referência.

Palavras-chave: CIGS, camada metálica, reflecção traseira, simulações óticas, TiW

Contents

List of figures

List of tables

Symbols

Symbol	Name	Unit
A	Diode ideality factor	
Ag	Silver	
Al_2O_3	Aluminium Oxide	
Au	Gold	
$a\text{-}Si$	Amorphous-silicon	
c	Free space light speed	m/s
Cu	Copper	
D	Displacement fields	C/m^2
E	Electrical fiel	V/m
$\|E\|^2$	Electrical field intensity	V/m^2
FF	Fill-factor	%
Ga	Galium	
H	Magnetic fields,	A/m
HfO_2	Hafnium oxide	
h	Planck constant	
In	Indium	
$I_{AM1.5}$	AM 1.5 Intensity	$W/m^{2\cdot}m^1$
J	Current density	A/m^2
j_0	Saturation current density	A/m^2
J_{SC}	Short-circuit current density	A/m^2
k	Boltzmann's constant	J/K
$MIBK$	Methyl isobutyl ketone	
Mo	Molybdenum	
$PMMA$	Polymethyl methacrylate	
P_{ABS}	Power absorbed per unit volume	$1/m^3$
q	Electronic charge	C
T	Temperature	K
Si_3N_4	Silicon nitride	
SiO_2	Silicon oxide	
Ta	Tantalum	
TiO_2	Titanium oxide	
TiW	Titanium-tungsten	
V_D	Applied voltage across the diode	V
V_{OC}	Open-circuit voltage	V
ω	Angular frequency	rads/s
W	Tungsten	
ZnS	Zinc sulfide	
η	Power conversion efficiency	%
ϵ''	Imaginary part of the dielectric permittivity	F/m
$\epsilon_Y(\omega)$	Complex relative dielectric constant	
ϕ	Photon flux	

Acronyms

AFM	Atomic Force Microscopy
Al:ZnO	Aluminium doped zinc oxide
CBD	chemical bath deposition
CGS	Copper Gallium Selenide
CIGS	Copper Indium Gallium Diselenide $Cu(In,Ga)Se_2$
CIS	Copper Indium Selenide
DWL	direct writing laser
EQE	External quantum efficiency
FDTD	Finite-Difference Time
INL	International Iberian Nanotechnology Laboratory
i-ZnO	Intrinsic zinc oxide
PV	Photovoltaic
PERC	Point Passivated Emitter and Rear Contact
RIE	reactive ion etching
SEM	Scanning Electron Microscopy
SLG	soda lime glass
TCO	transparent conducting oxide

Motivation and objectives

The main energy source for mankind has been burning fossil fuels. Despite being the most used source, it has two major limitations: it is i) a finite resource and ii) hazardous to the environment. The realization of its limitations fueled the search for energy sources that could mitigate these problems. Environmentally friendly technologies, also called green technologies, come as a solution to both fossil fuels limitations. Among the renewable technologies, there is the photovoltaic (PV) technology, in which the sun is used as an energy source. PV takes is name due to the photovoltaic effect, discovered in 1839 by Edmond Becquerel, where, the sun radiation is converted in electricity. Only in 1954, the first solar cell was produced at Bell laboratories [1], and since then commercial prices and production costs have been decreasing [2]. Despite the great progress achieve so far, for world-wide deployment of solar cells, there are two conditions that needs to be fulfilled: i) reduction of the production costs, and ii) an increase of the electrical performance [3].

Nowadays, research on solar cells is being performed to decrease the material consumption and increase the electrical performance of a solar cell. Thin film technology can fulfil such objectives, as it is able to achieve high electrical performance and a low material consumption [4],[5]. Currently, amorphous-silicon(a-Si), cadmium telluride (CdTe) and $Cu(In,Ga)Se_2$ (CIGS) are the most commercialized thin films technology [2] with light to power conversion efficiency world records of : 14 % , 22.1 % and 22.9 % respectively [6], [7]. A notable achievement was that CIGS solar cells were able to surpass multicristalline Si(22.3%) [6] on a laboratory level. Despite, being costlier right now, the productions costs of CIGS solar cells are dropping faster than silicon and with its conversion efficiency values continuing to rise, it is expected that this type of solar cell will be more widely used in the near future [8].

One of the main issues of CIGS technology is indium (In) scarcity which might raise production costs in the future [9].Reducing the CIGS thickness is of utmost importance to keep the technology cost-competitive. However, when decreasing the thickness down to the ultrathin range (around 500 nm) two major efficiency limiting problems arise; i) rear contact recombination [10] and ii) optical losses due to incomplete light absorption [10]. Recombination at the rear can be mitigated by incorporating a strategy that was first utilized in the Si technology of implementing point contacts with a passivation layer [3]. The major optical loss in a CIGS solar cells happens due to poor optical reflection of the rear contact, light reaching the contact is absorbed rather than reflected [11]. The metal chosen to increase the reflection at the rear must be done considering the high temperatures reached during the absorber growth. High optical reflective metals such as copper (Cu), gold (Au) and silver(Ag) are incompatible with the standard CIGS growth temperatures [12],[13].Orgassa *et al.* [14], reported that tungsten(W) and tantalum (Ta) can stand such temperatures and have presented promising results as a rear contact, however in ultrathin CIGS solar cells, to the author knowledge, these metals have yet to be tested.

The main objective of this thesis is to study alternative metals and metallic alloys to be applied at the rear contact of CIGS thin film solar cells in order to increase the rear optical reflection allowing for the use of ultrathin CIGS absorbers. For such purpose, a metal layer was deposited on top of the rear contact and below the passivation layer. In total six metals and two metallic alloys were tested and aluminum oxide (Al_2O_3) was the dielectric material used to passivate the rear CIGS interface. Complete solar cells were fabricated by partner institutions and analysed at INL, by J-V, external quantum efficiency (EQE) and reflections measurements. Optical simulations were done to theoretically, study which metal, theoretically, will have the most benefit regarding absorption of the incoming light in ultrathin CIGS layer.

1 Introduction

1.1 Solar cell parameters

A single junction solar cell is a device based on a p-n junction, which exhibits a behaviour of a diode. The electrical current that flows through a diode is calculated using the following equation [15]:

$$J = j_0 \left[exp\left(\frac{qV_D}{AkT} - 1\right)\right] \quad (1)$$

where J is the current density, j_0 the saturation current density, q the electron charge, V_D the applied voltage across the diode, A the ideality factor for a diode, k the Boltzmann's constant and T the temperature. In a more realistic model, this equation needs to be modified to include the series resistance(R_S) from ohmic losses at the interfaces and the shunt resistance(R_{SH}) from leakage current [16], the equivalent circuit with the series and shunt resistance is represented in **Figure 1.1a)**.

$$J = j_0 \left[exp\left(\frac{qV_D}{nkT} - 1\right)\right] + \frac{V_D - jRs}{R_{sh}} \quad (2)$$

A solar cell can be characterized by performing current density-voltage (J-V) measurements in the dark and in standardized illumination (simulation of sunlight). The parameters that describe a solar cell performance and that can be extracted from a J-V curve (**Figure 1.1b**) are: the short-circuit current density (J_{SC}), open-circuit voltage(V_{OC}) and fill-factor(FF).Together they are used to calculate the power conversion efficiency(η) of a solar cell [15]:

$$\eta = \frac{j_{mp}V_{mp}}{P_{inc}} = \frac{j_{sc}V_{oc}FF}{P_{inc}} \quad (3)$$

where, j_{mp} and V_{mp} the current density and voltage at the maximum power point (**Figure 1b**) and P_{inc} is the incident power.

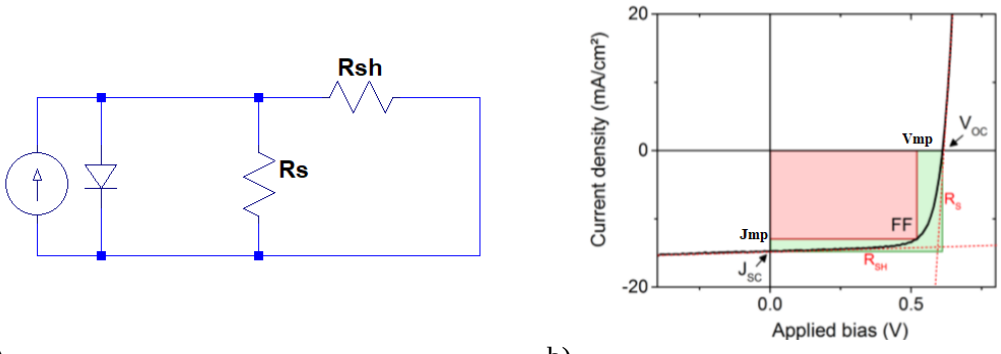

a) b)

Figure 1.1) A solar cell equivalent circuit;b) Current-voltage curve characteristics of a solar cell under illumination. Adapted from[17]

The V_{OC} is the point where the current density is zero, whereas the J_{SC} corresponds to the point where no voltage passes through cell. The fill-factor, is the ratio of the maximum generated power by a solar cell divided by the product of J_{SC} and V_{OC}, defined by [17]:

$$FF = \frac{j_{mp}V_{mp}}{J_{sc}V_{oc}} \quad (4)$$

External Quantum Efficiency (EQE) is a measurement that allows to evaluate the ability of a solar cell to convert the incoming light to photo-generated current. This type of measurement can identify the wavelength range where conversion losses occur [18], [19].

1.2 CIGS solar cell

A conventional CIGS solar cell structure and its layers are represented in **Figure 1.2**.

The usual substrate used for a CIGS solar cell is soda lime glass (SLG). SLG is cheap, thermally stable, has a smooth surface and an expansion coefficient close to the CIGS absorber, this is important due to the high temperatures reached during the CIGS absorber deposition [18]. SLG serves also as a sodium(Na) source, an element that improves the electrical performance of a CIGS solar cell [20].

Sputtered molybdenum(Mo) is used as the rear contact material for CIGS solar cells, due to several reasons; i) high melting point of around 2700 ºC, which allows to survive the harsh growth conditions of the absorber layer and ii)low diffusivity into the semiconductor films [19]. For Mo to achieve a good adhesion to the substrate and also a low resistivity, it is necessary to perform a bi-layer deposition [21]. The first deposition is performed at a high pressure to promote a better adhesion to the substrate surface and the second deposition at low pressure to reduce the film resistivity. One particular feature of Mo is it reaction with selenium [21]. A layer of MoSe2 will form at the interface with CIGS leading to a formation of a quasi-ohmic contact with CIGS [22].

The absorber will be discussed in detail later.

Following the absorber deposition, the formation of the p-n junction is assured with the deposition of a thin n-type buffer layer. Cadmium sulphide (CdS), deposited by chemical bath deposition(CBD) [21]. However, this layer has toxicity problems due to presence of cadmium and since it has a relativity low band-gap (2.4 eV) [19], some parasitic absorption occurs [11].Nonetheless, CdS, transmits most of incoming light to the absorber, it has a favorable band alignment with CIGS and forms a high quality p-n junction [21].

A transparent conducting oxide (TCO) is used for the window layer. The selection of which TCO to use must take into account the following conditions: i) formation of a transparent low resistant contact and at the same time a high resistant element to screen shunts and ii) create a favorable band alignment with the buffer layer [19]. Thus, to satisfy these conditions a by-layer is fundamental, being the first a thin layer with high resistivity, typically intrinsic zinc oxide (i:ZnO), the second layer with low resistivity, aluminium doped zinc oxide(Al:ZnO). Usually both layers are deposited by sputtering [21], however some alternate methods can be used [23], [24]. The i:ZnO will help to prevent any current leakage due to inhomogeneities. The Al:ZnO layer allows for high light transmission at minimum optical absorption [18].

The front contact is a stack of nickel(Ni)/aluminium(Al)/nickel(Ni), usually deposited by evaporation [21]. Depositing Al on top of Al:ZnO will dope the former layer, thus altering its proprieties [25]. Hence, a thin Ni layer is deposited to prevent the diffusion of Al and helps to protect the TCO layer. Since Al has a high malleability, it favors the electrical contact when doing measurements that use probes.

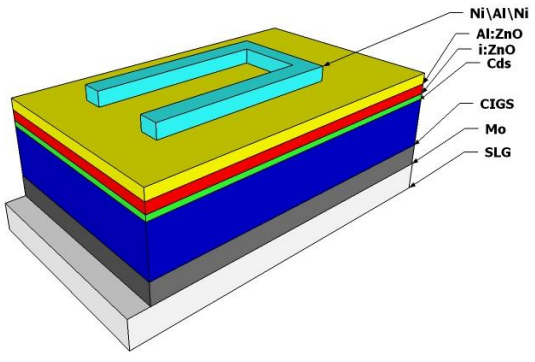

Figure 1.2 - Conventional solar cell structure, not at scale

1.2.1 State of the art

The story of CIGS began in 1975, at Bell laboratories when scientists achieved a power conversion efficiency value of 12%, by evaporating CdS on top of $CuInSe_2$ single crystal[26].

Research groups, stimulated by the results, began to develop different deposition process. Boeing and Arco solar had different deposition methods that achieved a good power conversion efficiency, Boeing was the first group to present a thin film device with more than 10% of power conversion efficiency, with a co-evaporation process, where Cu, In and Se were deposited from different evaporation sources [27]. Soon after, Arco solar, with a deposition-reaction process where Cu an In acted as metallic precursors and H_2Se the reacting chalcogen source, manage to achieved an higher power conversion efficiency value of 12 % with solar cells produced using the mentioned method. When the three-staged co-evaporation method invented by the National Renewable Energy Laboratories (NREL)[28], in 1994, provided the basis for 20 % in power conversion efficiency for a CIGS solar cell. Currently, this method is the most used deposition method for CIGS solar cells.

The effect of alkali elements on absorber layer has been a continuous research topic among the CIGS community, since it was first reported by Boeing in the 1980s [29]. However, the full effect of such materials in the absorber is not yet fully understood. Nonetheless, CIGS solar cells with a high power conversion efficiency use a three-staged co evaporation and incorporate alkali elements in the absorber layer[30], [31].

1.2.2 CIGS material

The CIGS compounds belong to the chalcogenide group. Chalcogenide materials are chemical compounds consisting of at least one chalcogen anion, a chemical element in column VI of the periodic table. One group of chalcogenides is the chalcopyrite crystal structure, which forms a tetragonal crystal structure (**Figure 1.3**) [32].

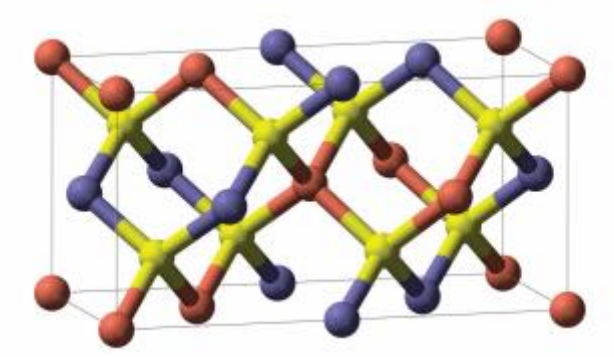

Figure 1-3 - The crystal structure of CIGS. The colours indicate copper (red), selenium (yellow) and indium (blue). The indium atoms can be replaced be Ga.[31]

Many chalcopyrite materials are semiconductors, of the type I-III-IV [31]. One of the most common chalcopyrite used for solar cells, is a compound containing a mixture of copper indium diselenide ($CuInSe_2$,CIS) and copper gallium diselenide($CuGaSe_2$,CGS), the compound resulting from this mixture is called ($Cu(In_xGa_{1-x})Se$, CIGS), where x can vary from 0 to 1 [15]. These compounds are remarkable by it capability of maintaining its crystal structure with significant changes in its chemical

composition [33].

CIGS is a p-type and direct bandgap semiconductor with a high value of absorption coefficient up to $10^5 cm^{-1}$ [19]. This high value of absorption coefficient allows the use of a thin layer(1-3µm) to achieve the same light absorption as multicristalline silicon which uses a much thicker layer, around 200µm. The electron diffusion length is low but it is in the order of the used thickness of CIGS [34].

CIGS has a self-doping nature, due to Cu vacancies. When it comes to the definition of CIGS properties, its Cu concentration is very crucial. Cu-poor CIGS, defined by the ratio ([Cu]/[Ga]+[In]) <1 , has smaller grains and presents good electrical performance.In contrast, Cu-rich CIGS, defined by the ratio higher than 1, has bigger grains and good crystalline properties although its electrical performance is weak comparing to the Cu-poor CIGS, caused by lower p-type doping and existence of $Cu_{2-x}Se$ [15], [35].

One interesting feature of CIGS compound is the ability to tune its bandgap to generate a quasi-electrical field by changing the gallium (Ga) gradient along the thickness of the absorber layer (replacement of In atoms of Ga) thus making its bandgap values range from 1.02 to 1.68eV [19].

1.3 Passivation effect

The major electrical losses that CIGS solar cells have are bulk and interface recombination, limiting the solar performance [10].

A way to reduce the recombination of the rear is by Ga grading [36]. By adjusting the quantity of Ga at the rear, it creates a quasi-electrical field that forces the minority carriers away from the rear thus reducing the recombination.

The interface recombination can be addressed with the introduction of a passivation layer, normally an insulator, at the interfaces. This passivation effect can be split in two: i) chemical passivation, a term originated from the Si technology, this type of passivation decreases the number of active defects at the interface [37]; ii) field-effect passivation, the passivation layer has a high number of fixed charges, which produces a field effect that repels the minority carriers [37].When addressing the recombination at the rear with a passivation layer, an optical effect occurs as the rear optical reflection [37]increases, however this enhancement is insufficient for fully enhancing the light absorption in the CIGS layer [36].

The first mention of the use of a passivation layer alongside with nano-size point contacts was done by *Green et al* [3] by introducing the so-called Point Passivated Emitter and Rear Contact solar cell structure (PERC) [3]. In silicon solar cell technology this allowed the increase of the V_{OC}. This structure is described in **Figure 1.4**. It allows for a reduction in the rear recombination by decreasing the contact area between the metal and semiconductor along with the passivation layer.

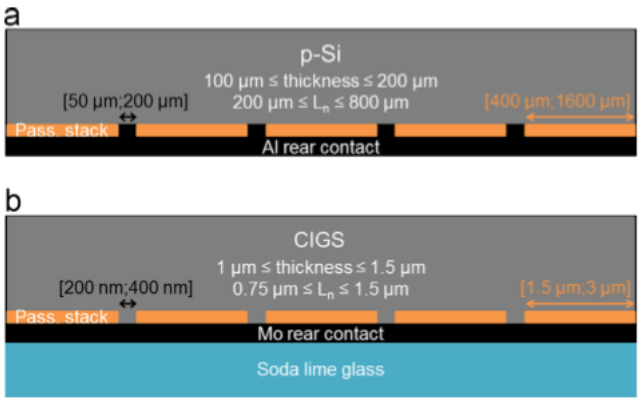

Figure 1.4 - Schematic representation of the rear of (a) a p-type Si solar cell with a surface passivation stack and micron-sized local point contacts and (b) CIGS solar cell with a surface passivation stack and nano-sized local point contacts. Also the typical base/absorber thickness, minority carrier diffusion length, contact opening diameter and distance between contact openings are specified [34].

However, when bring the PERC structure to CIGS solar cells, the diffusion length of the minority carriers has to be taken in to account in order to determine the better dimensions of the point contacts[34].

In a recent study, *Salomé et all* [37] ,demonstrated, once again [38], the passivation effects of Al_2O_3,where the solar cells that incorporate the dielectric showed higher figures of merit than the solar cell with no dielectric material. Due to the good results achieved, Al_2O_3, will be used as the dielectric material on this thesis. Other materials are also being tested as passivation material such as titanium oxide (TiO_2) [39], zinc sulfide (ZnS) [40] and some dielectrics materials like hafnium oxide(HfO_2) , silicon oxide(SiO_2), silicon nitride (Si_3N_4) are also mentioned in the literature [29],[41].

2 Materials and methods

The main objective of this work is to increase the optical refection at the rear of a CIGS solar cell, by depositing metals on top of the rear contact and below the dielectric layer. The metals were chosen based on their optical properties as well as their availability at the INL cleanroom deposition systems. Thus, six metals Ag,Au,Cu,Ta, Ti and Zn and two metallic alloys, titanium-tungsten (TiW) and AlSiCu are tested. The dielectric to passivate the interface will be Al_2O_3 and the nanopatterning will be defined by e-beam lithography and reactive ion etching(RIE).

The following sub-chapter will focus on the fabrication steps until the absorber growth. The remaining fabrication of the solar cells, a standard baseline process, was done by collaborators at Uppsala University in Sweden. After fabrication, the cells are shipped back to INL for further characterization.

2.1 Solar cell fabrication and deposition techniques

Here at INL, we focus in the modification of the rear structure in a CIGS solar cell, as such in this work the fabrication occurred after the Mo deposition and before the CIGS growth (**Figure2.1**), whereas the remaining fabrication of the solar cell was to be done at Uppsala University in Sweden.

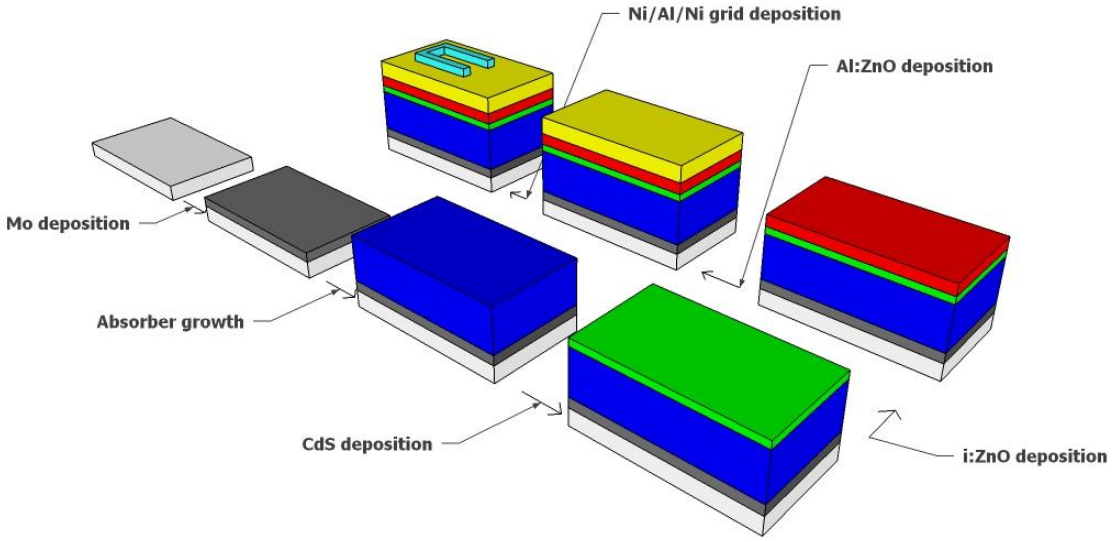

Figure 2.1 - Standard step by step fabrication for a CIGS solar cell. In this thesis the fabrication will occur between the Mo deposition and the absorber growth. Not on scale

The rear contact, a 350 nm Mo layer, was deposited at Uppsala University using a DC-sputtering system in a vertical inline MRC 603 tool, with a DC power of 1500 W, on top of 5x5 cm^2, 2 mm thick SLG. Afterwards, the samples are shipped to INL. Upon arrival, all samples went through a cleaning process. The process consisted of consecutive ultrasound baths in acetone (10 minutes), followed by isopropanol (10 minutes) and then di-ionized water (5 min).

Afterwards, 20 nm of metal was deposited on top of the Mo layer using DC sputtering in different tools:

i) For the deposition of Ag, Au, Cu, Ta, Ti and Zn, a Kenosystec- ultra high vacuum tool (UHV) multitarget confocal sputtering tool is used. The DC power was of 400 W, the base pressure was $1x10^{-8}$ mbar, the deposition pressure was $9.1x10^{-3}$ mbar;

ii) The metallic alloys, TiW and AlSiCu were deposited using a Metallization Singulus Sputtering tool ,Timaris FTM. The substrate temperature is not intentionally increased, however, due to the proximity to the target, it can reach temperature values as high as 200 ºC, which depends on the deposition time.

After the metals deposition, 18nm of Al_2O_3 was deposited by RF sputtering using the same tool for the metallic alloy deposition. This was possible due to the possibility of the tool to operate in DC and RF mode.

To create the desired pattern, e-beam lithography was used, the pattern consists of a square array of 200 nm diameter holes with a pitch of 2µm. The pitch is defined as the inter-distance between the start of two consecutive holes.

The lithography process starts with the coating of the samples with a photoresist (PR) designated by polymethyl methacrylate, commonly called PMMA. A Suss Microtec Gamma Cluster track tool was used to deposit the resist. In this system, the PR must be inserted in a syringe and then manually introduced in the track. The deposition of 430 nm PMMA was done by spin-coating for 1 minute followed by a hard-bake at 150 ºC for 1 minute. The samples are exposed using electron-beam lithography system, Vistec 5200 ES 100 with a beam current of 96 nA and an acceleration voltage of 100 kV. Such exposure is very time-consuming, as the exposure for 1 sample takes ~12 hours to complete. After the exposure, the samples were developed. The development is done with a Suss track, the developer used is Methyl isobutyl ketone (MIBK) and the each sample development takes 40 seconds.

Afterwards, to create nano-sized point contacts a reactive ion etching (RIE) is done through the resist, the dielectric and the metal, using a SPTS ICP system who relies in chlorine ions to etch through the materials. The etching was done for 45 seconds, for all samples that went through the lithography process, a helium gas is used for aiding the backside cooling of the sample. After the etching, the samples were risen with water to prevent any further etching of chlorine ions.

Finally, to remove the unexposed resist, the samples were bathed in acetone and left at the ultrasounds for 20 minutes. After that, the procedure is repeated using deionized water for 5 minutes. **Figure 2.2a**) shows the structure before the absorber deposition and in **Figure 2.2b)** a schematic represents the fabrication steps.

a)

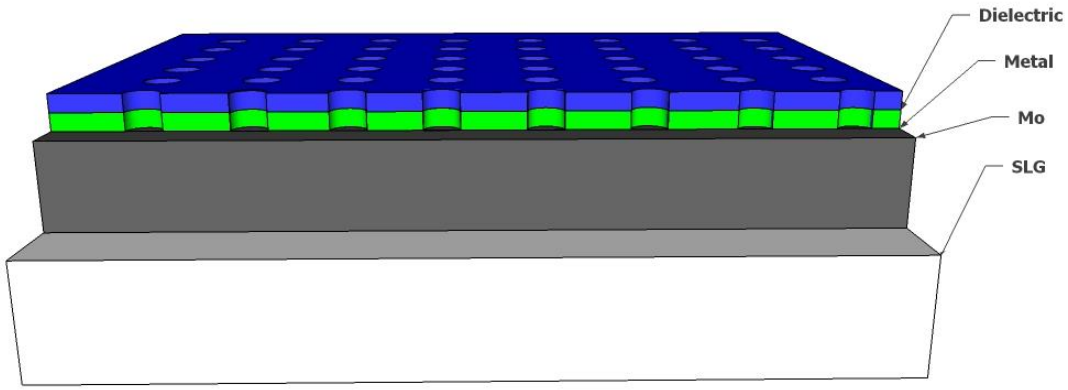

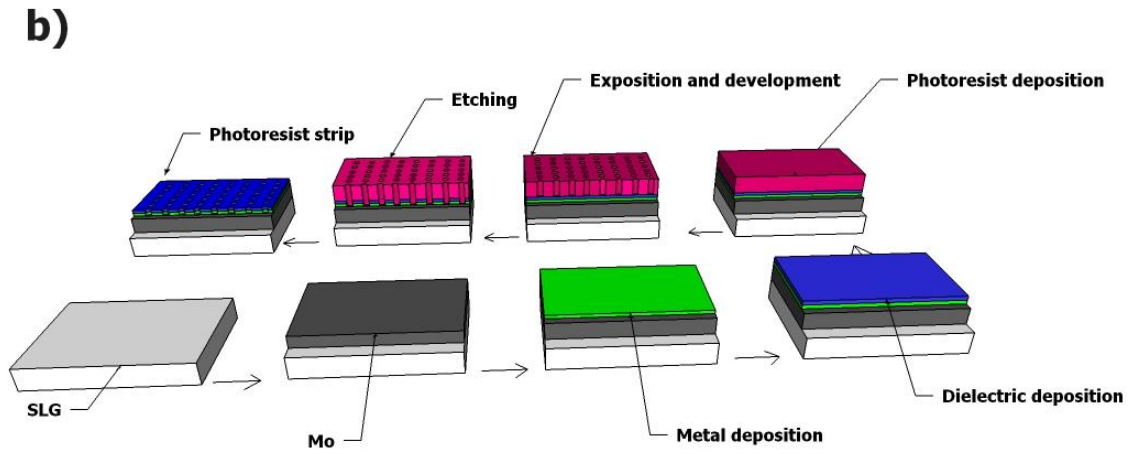

Figure 2.2 - a) Representation of the structure obtained after the resist removal; b) Schematic showing the fabrication steps. Both figures are not on scale

The samples are then shipped to Uppsala to complete the solar cells fabrication, following the Angstrom solar cell baseline [21]. A CIGS layer was co-evaporated at 550 ºC. A Ga flat gradient was used to prevent a Cu and Ga depth profile. The composition of the CIGS is: [Cu]/[Ga]+[In] = 0.90 and [Ga]/[Ga] + [In] = 0.30.

Thirteen sets of solar cells were then made, where two sets are regular CIGS solar cells, designated as reference with a structure: Mo\CIGS\CdS\i:ZnO\Al:ZnO\Ni/Al/Ni grid, two sets incorporate Al_2O_3 with the following structure: Mo\$Al_2O_3$\CIGS\CdS\i:ZnO\Al:ZnO\Ni/Al/Ni grid. The remaining eleven sets will use the metal layer as well as Al_2O_3, with the following structure: Mo\Metal\$Al_2O_3$\CIGS\CdS\i:ZnO\Al:ZnO\Ni/Al/Ni grid. The sample names as well the summarized information is found in **Table 1**.

Table 1 - Summarized information of the samples produced in this work as well as their naming

Pitch: 2 µm; **Hole diameter**:200 nm; **Al_2O_3 thickness**:18 nm; **Metal thickness**: 20 nm		
Metal	**Number of samples**	**Sample name**
Only with Al_2O_3	2	Mo/Al_2O_3-I; Mo/Al_2O_3 -II
TiW	2	Mo/TiW/Al_2O_3-I; Mo/TiW/Al_2O_3 -II
Au	1	Mo/Au/Al_2O_3
AlSiCu	1	Mo/AlSiCu/Al_2O_3
Ta	1	Mo/Ta/Al_2O_3
Ti	1	Mo/Ti/Al_2O_3
Zn	1	Mo/Zn/Al_2O_3
Cu	1	Mo/Cu/Al_2O_3
Ag	1	Mo/Ag/Al_2O_3
Reference samples	2	Reference -I; Reference -II

2.2 Characterization techniques

In this section, the characterization techniques used in this work are described. The samples are characterized at two stages in their production. Before the CIGS deposition, the surface is characterized and the samples relative optical reflection is measured. After complete solar cell processing, the cells were characterized by J-V, EQE and relative optical reflection measurements.

For the surface analysis, Scanning Electron Microscopy (SEM) was performed. A

NovaNanoSEM650 system was used, with an acceleration voltage of 5kV.

Morphology analysis was done using Atomic Force Microscopy (AFM), on tapping mode and with a scan rate of 1Hz in the system AFM Dimension Icon.

To measure the relative optical reflection UV-VIS NIR Spectrophotometer was used using an integrating sphere. The wavelength range used was from 300 to 1100 nm with a step of 10 nm.

The J-V measurements were performed in Uppsala university, using a home-made J-V system. Where a tungsten halogen lamp was used. The lamp was calibrated, with a certified silicon photodiode from Hamamatsu Photonics to give the same amount of photon as in AM1.5 light with an intensity of $1kW/m^2$. The voltage range was from -0.5 V to 1 V with a step of 50 mV.

EQE measurements, done at INL, were performed using a solar cell efficiency measurement system QEX10, with a monochromatic light scanned trough the wavelength interval of 300 nm to 1100 nm with a step of 10 nm.

The optical simulations were done employing 3D a Finite-Difference Time domain (FDTD) using a commercial software *Lumerical*.

This method solves Maxwell's curl equations in arbitrary geometries and materials. The equations are the following [42]:

$$\frac{\partial \boldsymbol{D}}{\partial t} = \nabla \ \boldsymbol{H} \tag{5}$$

$$\frac{\partial \boldsymbol{D}}{\partial t} = \nabla \ \boldsymbol{H} \tag{6}$$

$$\frac{\partial \boldsymbol{H}}{\partial t} = -\frac{1}{\mu_o} \nabla \ \boldsymbol{E} \tag{7}$$

where **H**,**D** and **E** are the magnetic, displacement and electric fields, respectively, while $\epsilon_\gamma(\omega)$ is the complex relative dielectric constant ($\epsilon_\gamma(\omega) = n^2$, where n is the refractive index).

Due to the periodicity of the square array of rear point contacts,2µm pitch, we can reduce the FDTD region to a square unit cell with a 2µm side. Specific boundary conditions (BCs) were applied in each face of such region. Artificial absorbing perfect-matching layers were applied on the upper and lower boundaries to absorb all outgoing waves. On the side boundaries, periodic BCs were used to model the infinite periodicity of the structures. Here, due to the symmetries of the structure at normal incidence, symmetric and antisymmetric BCs were employed, which allow simulating only one quadrant of the unit cell.

To simulate solar illumination, a broadband plane wave source is placed in the medium above the structure, with a bandwidth of: 300-1100 nm.

3 Results and discussion

In this chapter, each result will be shown and discussed.

First, to analyse the optimum optical behaviour of the solar cells produced in this work as well as the optical influence of the metal layer, optical simulations were conducted using the commercial software *Lumerical* and its results are presented and discussed.

The samples are analysed by SEM images, prior the absorber growth to ensure that the hole diameter has the expected dimension and the optical relative reflectance was also measured.

The solar cells are then analysed by optical relative reflectance, J-V and EQE measurements.

3.1 Numerical model

The optical properties of the materials utilized in our structures are determined by the values of complex refractive index(n,k). For the materials, Au,Ag,Cu,Al_2O_3 and Ti , the complex refractive index values were taken from ref [43], for Ta and Zn the values were taken from ref [44] , for AlSiCu it was from ref [45] the values for CIGS with [Ga/(Ga+In)] =0.30 were taken from ref [46].Unfortunately, the optical ellipsometry results for TiW did not arrive in time to be included in the optical simulations.

The power absorbed per unit volume (P_{ABS}) in each element of the structure used in the optical simulations is given be the resulting electric field distribution established in their material:

$$P_{ABS} = \frac{1}{2}\omega\epsilon''|\boldsymbol{E}|^2 \tag{7}$$

where, ω, is the light angular frequency,ϵ'' is the imaginary part of the dielectric permittivity and $|\boldsymbol{E}|^2$ is the electrical field intensity. P_{ABS} is normalized by the source power to obtain the absorption per unit volume, p_{ABS}. The total light absorption in a region, at a certain wavelength(λ) is computed by integrating p_{ABS} over its volume:

$$Abs(\lambda) = \int p_{ABS} dV \tag{8}$$

In the solar cells produced in this work, only light absorbed in the CIGS layer leads to photocurrent. Thus, in the simulations we integrate p_{ABS}, only in this layer, since light absorbed in the other layers leads to parasitic absorption resulting in optical losses. Trough, the integration of p_{ABS} on the CIGS layer and the assumption that every photon absorbed in the CIGS layer generates carriers, the software can calculate J_{SC} values. Hence, J_{SC} values are determined integrating the absorption in the CIGS layer with the incident AM1.5 solar power spectrum, over the desired wavelength range (300-1100 nm):

$$J_{SC} = q\int \frac{\lambda}{hc} Abs(\lambda) I_{AM1.5}(\lambda) d(\lambda) \tag{9}$$

where, q is the electronic charge, h is the Planck constant and c is the free space light speed. The wavelength interval was chosen between these values as light outside this interval does not contribute to the photo-generated current: light with energy higher than 300 nm is absorbed in the windows layers; light with energy below 1100 nm is below the bandgap of the CIGS used in this work ,1.2 eV. The determination of the CIGS bandgap is shown in **Annex A.** The J_{SC} values calculated can be regarded as optimal, as it does not consider any electrical losses or other experimental situations such as: roughness, interfaces, elemental diffusion, light scattering at grain boundaries, among others. For a more detailed description on the numerical methods, the reader is pointed to refs [42], [47], [48].

The optical simulations conducted in this thesis, are presented in the following sub-chapters. We will start with the identification of optical losses in ultrathin CIGS layer by comparison with a thick counter-part. Then, a solution to address these losses is presented and discussed.

To simulations precision is observed by performing a comparison between the FDTD result and

the Transfer Matrix analytical formalism. If both plots overlap the simulation has a good precision level. This comparison is seen in **Figure 6.2**. For simplicity, only one plot is shown as all present simulations present qualitatively good overlaps.

3.1.1 Optical characteristics with ultrathin absorber

In this section, we compare the optical characteristics of our 500 nm absorber ultrathin reference solar cell with a 500 nm absorber with a standard-thick solar cell possessing a 2 µm thick CIGS layer. In the simulations, the only difference between the cells is the absorber thickness, the remaining layers have the same thickness value.

The simulations results are present in **Figure 3.1a,b)**, where the CIGS, solar cell absorption, reflectance and Mo parasitic light absorption of the simulated solar cells are shown, and the results are summarized in **Table 2**. Henceforth, when the author mentions reflection it regards only the optical reflection, any other form of reflection will be properly identified. Ultrathin devices have high optical losses due to a low absorption values for wavelengths higher than 600 nm as verified experimentally [10]. This is clear in **Figure 3.1a)**, as the light absorptance for the ultrathin solar cell decays very fast for the wavelength mentioned above. The optimal J_{SC}, discarding any electrical losses, for the 2µm solar is 33.85 mA/cm^2 and for the ultrathin solar cell 30.03 mA/cm^2. Thus, the difference between the absorber layers thickness is responsible for a 3.82mA/cm^2 optical loss. Note once again, that this difference only accounts for optical considerations, excluding electronic ones which are responsible for significant losses as well [10], [37]. It should also be noted that the thick solar cell is relatively simple compared with the CIGS state-of-the-art cells that present Ga values dependent on depth and several front interface modifications that heavily change the absorption properties. Such aspects explain the lower value of the simulations compared with the world-record values (~36 mA/ cm^2) [6].Furthermore, from **Figure 3.1b)**, the solar cells reflectance differs for wavelength value higher than 1000 nm, with the standard-thick solar cell with 2 µm CIGS having a poor reflectance. This is due to: i) the solar cell stack does not reflect much of the incident light since the refractive index gradient of the materials present in the solar cell stack are beneficial for anti-reflective properties [49]; ii)the absorber being thick enough to absorb the incoming light and no losses occur due to reflection of the rear contact. For an ultrathin solar cell, when the light absorption in the CIGS layer decreases, the parasitic absorptance at the rear contact increases. Indicating that most of the light that reaches the rear is absorbed by the contact. Such optical loss was already reported in the literature [10], [14]. The parasitic light absorption at the rear contact is also present for a regular solar cell, however due to the thickness of the absorber only a small fraction is absorbed .According with our simulations, 2.42 mA/cm^2 is absorbed at the rear for an ultrathin solar CIGS solar cell and 0.25 mA/cm^2 for a regular CIGS solar cell, these values matches with the ones simulated by *Orgassa et all* [14].

A possible solution to decrease such optical loss and enhancing the rear reflection, is proposed in this work, with the simulations results of the proposed solution being presented in the next section.

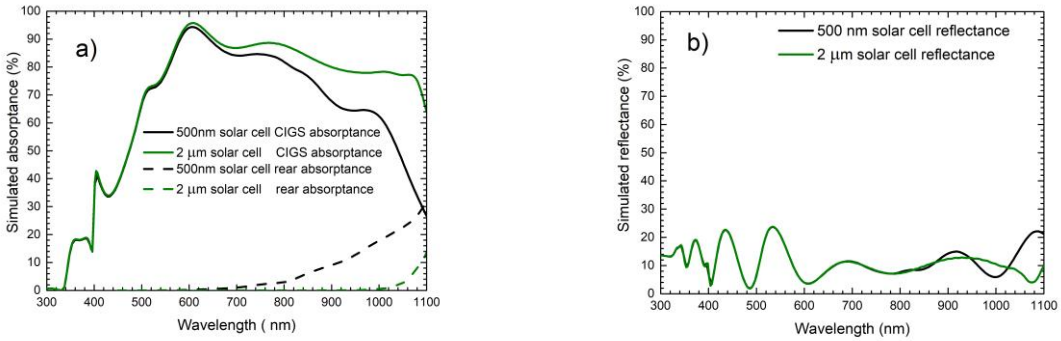

Figure 3-1 - a) simulated CIGS absorptance for an ultrathin solar cell and a regular solar cell with a 2µm absorbed layer (solid lines), parasitic light absorptance at the rear contact (dashed lines); b) simulated solar cell reflectance for ultrathin solar cell and a regular solar cell with a 2µm absorbed layer. The calculated J_{SC} for the ultrathin solar cell was of 30.03 mA/cm^2 and 33.85 mA/cm^2 for the standard solar cell

3.1.2 Simulations for solutions of increasing the rear reflection at the rear contact

In the previous section the parasitic light absorption at the rear was identified as the main optical loss of an ultrathin solar cell. Thus, this section will focus on a modification to the solar cell architecture that could address this issue. A metallic layer will be incorporated between the rear contact and the dielectric material (Al_2O_3). The simulation is done using the solar cells structures fabricated in this work. The simulation results are shown in **Figure 3.2**, and the J_{SC} values calculated are represented in **Table 2**. All solar cells that incorporate a metal layer at the rear, show an enhancement in the CIGS light absorptance for wavelengths higher than 600 nm, over the reference solar cell, with the solar cell with no metal layer giving the worse CIGS light absorptance as seen in **Figure 3.2.a)**. The increase in the amount of light absorbed at the CIGS layer is due to the poor optical reflectivity of the rear metal (Mo). The enhancement is higher for solar cells that incorporate lower refractive index metals (**Figure 6.3**), as such the Mo/Ag/Al_2O_3 solar cell shows the highest enhancement in light absorptance at the CIGS layer and with an optimal J_{SC} of 32.05 mA/cm^2.Only the solar cell Mo/Ti/Al_2O_3 gives the lowest J_{SC} value of the solar cells simulated with a metal layer, 31.01 mA/cm^2. The J_{SC} values for the Mo/Ti/Al_2O_3 solar cell is in fact lower than the one of the Mo/Al_2O_3 solar cell, 31.15 mA/cm^2. The three solar cells, Mo/Ag/Al_2O_3, Mo/Au/Al_2O_3 and Mo/Cu/Al_2O_3, show the highest enhancement of light absorptance in the CIGS layer compared with the reference solar cell, being very promising as they increase the J_{SC} from the reference solar cell from 30.03 to 32.05 mA/cm^2, 31.98 mA/cm^2, 31.95 mA/cm^2, respectively.

Simulations were conducted to study the influence of the metal layer on the parasitic light absorptance at the rear. Hence, we simulated the absorptance at the rear (Mo+Metal), assuming no absorptance in the dielectric layer, with the results shown in **Figure 3.2b).** Considering this simulation, the solar cell Mo/Ti/Al_2O_3 has a parasitic light absorptance, similar to the reference solar cell. Such absorption is due to the fact that 20 nm of Ti are enough to enhance the parasitic light absorptance and degrading the optical properties of the solar cell. The parasitic light absorptance in this solar cell is responsible for a loss of 2.22 mA/cm^2. Apart from Mo/Ti/Al_2O_3 solar cell, all of the combinations show a significant reduction in the parasitic light absorptance at rear contact. Even the simple introduction of the dielectric layer diminishes this losses, which was already confirmed experimentally [37], [38]. From **Figure3.2a**) we see that the increase in the light absorptance in the CIGS layer does not correspond to the increase in reflectance for the same wavelength regions, thus some of reflected light leaves the solar cell rather than being absorbed in the CIGS layer as shown by an increase of the reflectance at the wavelength values above 900 nm as seen in **Figure 3.2c)**.

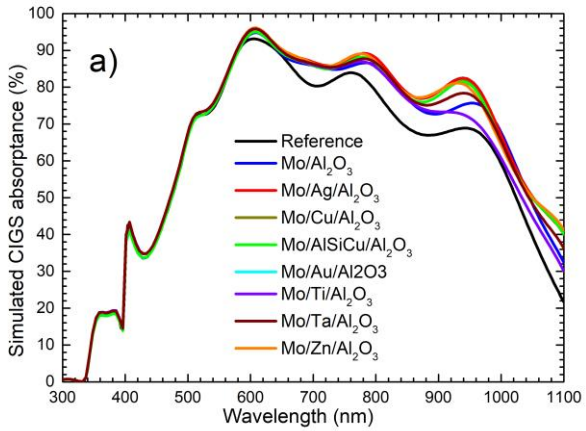

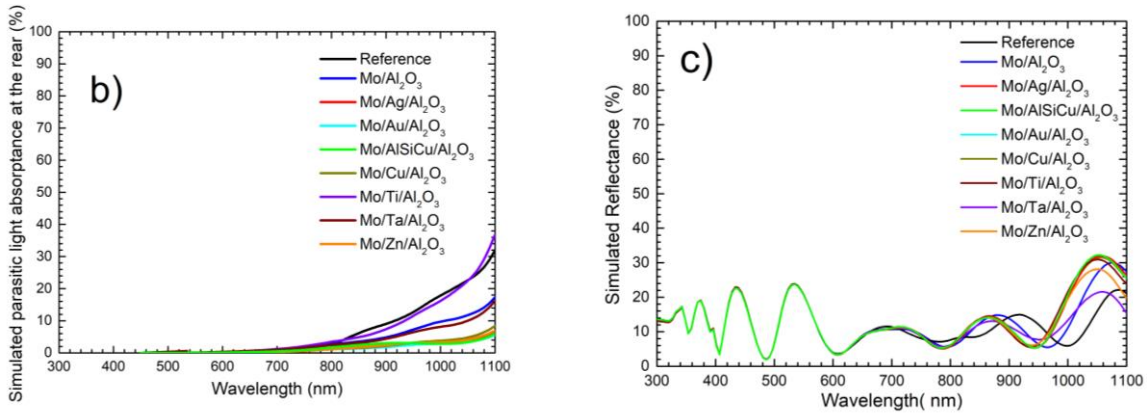

Figure 3.2 a) CIGS absorptance for all solar cells simulated; b) total solar cell reflectance for the solar cells simulated; c) parasitic light absorptance at the rear contact for the simulated solar cells.

One additional study done in these simulations, was to compare the performance of the solar cells with the highest light absorptance ,Mo/Ag/ Al_2O_3, with the regular solar cell, as presented in **Figure 3.3**.The light absorbed in the CIGS layer in the Mo/Ag/ Al_2O_3 surpasses the regular solar cell for certain wavelengths(~700 and 800 nm), however for wavelengths higher than 900 nm the Mo/Ag/ Al_2O_3 starts to underperform. This loss accounts for a difference of 1.3 mA/cm^2 in the J_{SC} between the solar cells. Such current loss is due to light reflected at the rear leaving the solar cell, hence, to reach the J_{SC} values of a regular solar cell, light trapping schemes should be also used to promote a longer light path [50], [51]. However, if these reflectance values can be reached with a CIGS thickness reduction of 75% (from 2000 to 500 nm) without compromising on the other figures of merit of the solar cell, a significant cost reduction in the solar cell production could already be achieved. Nonetheless, these simulations assume that the metals survive the harsh CIGS growth conditions, unfortunately, some of these metals are known to easily react with the CIGS and with Se [12]–[14]. Therefore, the technical capability of producing these architectures needs to be experimentally tested.

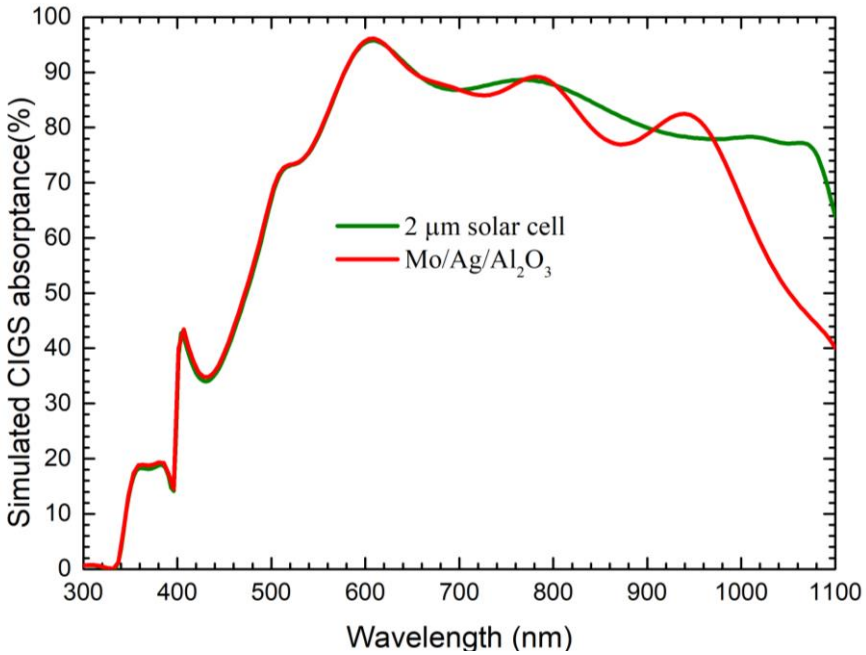

Figure 3.3 - CIGS absorptance for a regular solar cell with a 2µm CIGS solar cell and for the ultrathin solar cell with Ag as a metallic layer (Mo/Ag/Al2O3)

Table 2 - Simulated J_{SC} for all solar cells simulated as well as the J_{SC} absorbed at the rear contact

Simulated solar cell	Colour in the plot	J_{SC} given by the optical simulation (mA/cm^2)	Parasitic light absorption at the rear (Mo+Metal) (mA/cm^2)
Reference		**30.03**	**2.42**
Mo/Al_2O_3		**31.15**	**1.30**
$Mo/Ag/Al_2O_3$		**32.01**	**0.51**
$Mo/AlSiCu/Al_2O_3$		**31.85**	**0.57**
$Mo/Au/Al_2O_3$		**31.98**	**0.49**
$Mo/Cu/Al_2O_3$		**31.95**	**0.59**
$Mo/Ti/Al_2O_3$		**31.01**	**2.22**
$Mo/Ta/Al_2O_3$		**31.60**	**1.10**
$Mo/Zn/Al_2O_3$		**31.80**	**0.54**

3.2 Sample fabrication

To increase the rear reflection of an ultrathin CIGS solar cell, the standard rear structure of such solar cell must be modified. Thus, in this work, a metallic layer, 20 nm, is deposited on top of the rear contact, Mo and below the dielectric layer, 18nm of Al_2O_3 is used. To establish, contact between the CIGS layer and the rear contact, a pattern consisting of a square array of 200 nm holes with a pitch of 2µm is created by e-beam lithography. RIE is then used for opening the point-contacts. For more detailed information of the solar cells fabrication used in this work, the reader is directed to **Section 2.1.**

The following section will focus on the characterization of the fabricated samples, before the CIGS growth. Top view SEM images were taken to verify if the point-contacts were successfully open and relative reflection measurements were conducted to verify the samples reflectance.

3.2.1 Substrate characterization

To verify if the e-beam exposure and the etching steps were successful in the formation of the point-contacts, top view SEM images were taken of all the samples, as shown in **Figure 3.4.** For simplicity, only the images for samples Mo/Al_2O_3 and $Mo/TiW/Al_2O_3$ are shown, as the desired pattern was obtained in all samples. The application of e-beam lithography was able to generate the point-contacts on the Al_2O_3(18nm) and the metal layer (20 nm). All samples have the expected pitch of 2µm, however, we note that the holes form an elliptical shape rather than circular, causing the dimensions to be elongated in a particular direction. The modification in the holes form as well as in their dimension is attributed to an imperfection in the electron optics, in particular, astigmatism, that occurs in the exposure, leading to an elongation in a privileged direction. However, the e-beam process, could form point-contacts more cylindrical with a higher exposure time. Since, a 5x5 cm^2 already takes 12 hours to expose, we need to compromise exposure time with the point-contacts shape. The dimensions obtained do not make a constraint in the solar cell performance [37]

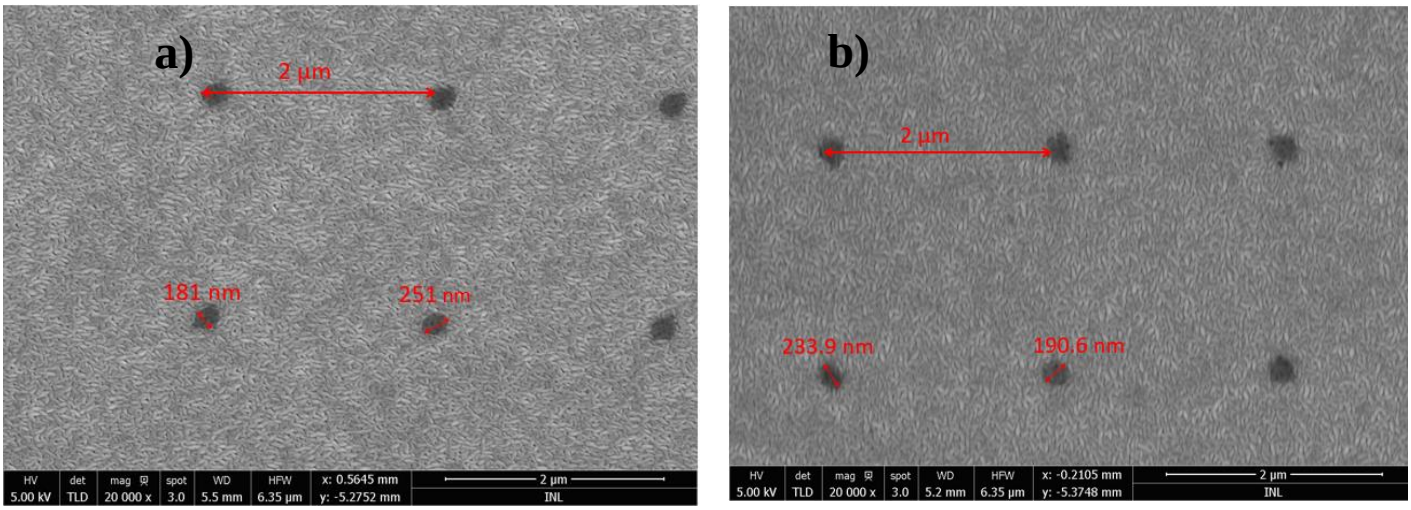

Figure 3.4 -SEM top-view images of the samples Mo/Al2O3 (a) and Mo/TiW/Al2O3 (b). The images show the pitch dimensions as well as the hole diameter. A expected 2µm pitch is achieved, the hole diameter is elongated in a particular direction due to e-beam astigmatism.

In **Section 3.1** we identified that the poor reflection of the rear contact material as the main optical loss in an ultrathin CIGS solar cell. Hence, relative reflectance measurements were done to evaluate the reflectance of the samples prior to the absorber growth (**Figure 3.5)**. The samples $Mo/Ag/Al_2O_3$, $Mo/Au/Al_2O_3$,and $Mo/AlSiCu/Al_2O_3$ present the highest reflectance values for wavelengths higher than 800 nm and, on the other hand, $Mo/Ti/Al_2O_3$ and $Mo/Ta/Al_2O_3$ having the lowest reflectance in the same wavelength region. We should note that the interface: Al_2O_3/air is very different from Al_2O_3/CIGS due to a higher refractive index of the absorber material. Hence, interfaces with the refractive index(**Figure 5.3**) closer to the refractive index of air (n=1), present the lowest reflectance in this measurement.

From these measurements, the samples $Mo/Ag/Al_2O_3$, $Mo/Au/Al_2O_3$ and $Mo/AlSiCu/Al_2O_3$ show the best results in the reflective reflectance, however these metals are known to react very easily with CIGS and Se [12]–[14]. The sample $Mo/TiW/Al_2O_3$, shows the most promising results: i) this metal was tested as back contact for CZTS solar cell, with significant results [52];ii) has high relative reflectance and iii) is stable at high temperatures [53], [54].

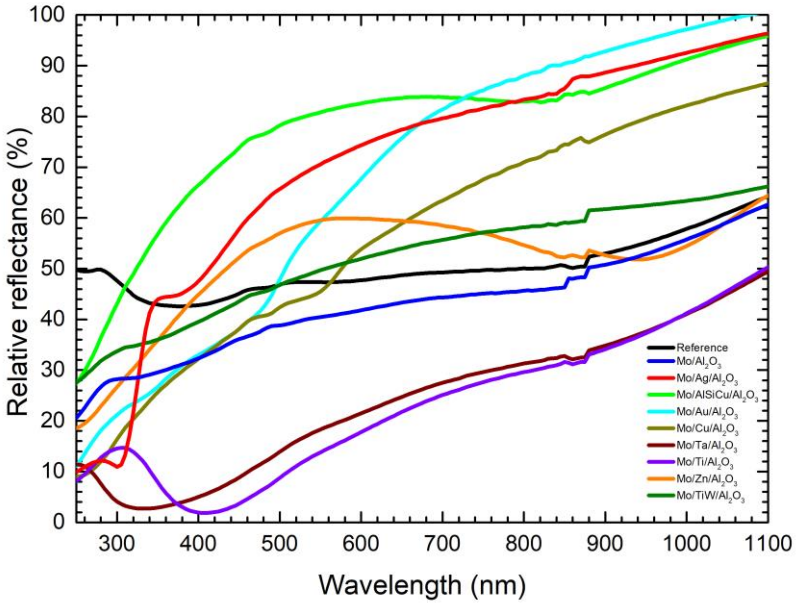

Figure 3.5 - Measured reflectance of all the samples fabricated prior to the absorber growth. A kink is observed at around 900 nm, due to a change in the detector in the system. Reflectance relative to a BaSO4 reference.

3.3 Solar cells characterization

Upon arrival at Uppsala University, the samples are cut in two pieces of 2.5x5 cm^2, to compensate for any mistakes that could occur during the solar cell processing.

Three samples did not survive the complete solar cells process; the CIGS layer in Mo/TiW/Al_2O_3, suffered a partial peel-off during the CdS deposition, however, this occurrence might be linked with high NaF thickness [55]; in Mo/AlSiCu/Al_2O_3 sample, during the CBD, particles agglomerated on the sample surface, something that is not yet understood. Still, the solar cells fabrication was successful on the remaining 13 samples, with the results being shown and discussed in the following section. Each sample produced 16 solar cells, with an area of 0.5 cm^2 per solar cell.

3.3.1 Solar cells relative reflectance

The relative reflectance of the solar cells fabricated is shown in **Figure 3.6**.

From **Figure 3.6** we note that of the samples that showed the highest reflectance in **Figure 3.5** (Mo/Au/Al_2O_3, Mo/Ag/Al_2O_3, and Mo/Cu/Al_2O_3), only the sample Mo/Au/Al_2O_3 has a relative reflectance higher than the reference solar cell, indicating remarkable differences in the solar cell stack that appeared during the experimental fabrication. The Mo/Ag/Al_2O_3 solar cell shows a similar compared to the reference solar cell. For the Mo/Cu/Al_2O_3, the reflectance is only higher than the reference solar cell for the wavelength interval between 800 and 900 nm. The difference in the relative reflectance of the solar cells with the corresponding samples reflectance could be an indication of diffusion of such metals (Ag,Cu) to the CIGS. This changes the rear layers uniformity, affecting the reflectance. The relative reflectance of the solar cells Mo/Al_2O_3 and Mo/Zn/Al_2O_3 is higher than of the reference solar cell, showing an agreement with the simulated reflectance (**Figure 3.2c**). The solar cell

$Mo/Ti/Al_2O_3$ shows the second highest reflectance, which does not match the simulated reflectance of such solar cell. The difference could be attributed to the reaction of titanium with Se, forming $TiSe_2$ [56] a compound with high reflectivity for wavelengths higher than 900 nm [56], possibly explaining the difference between the simulated and measured reflectance for this solar cell.

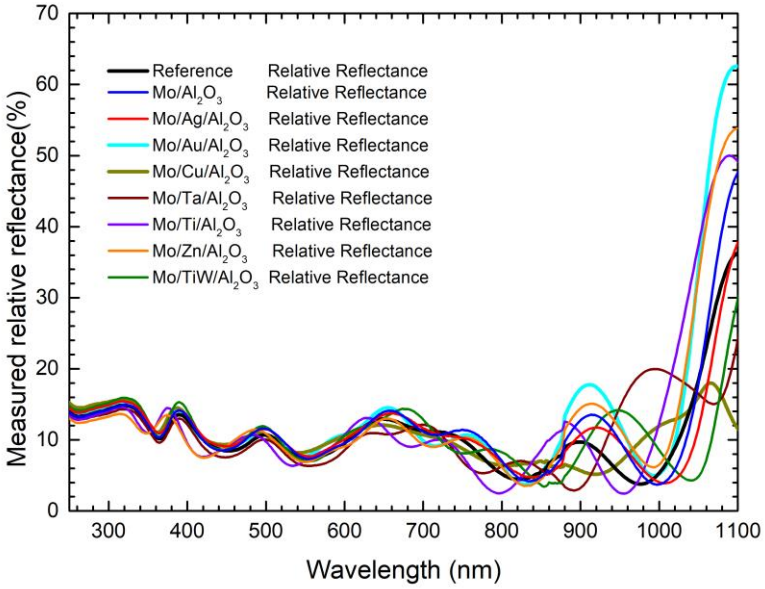

Figure 3-6 – Measured relative reflectance of the solar cells fabricated.

3.3.2 Electrical characterization

J-V and EQE measurements were done for the solar cells that survived the fabrication process, with the representative illuminated J-V curves being shown in **Figure 3.7a),b)**. In **figure 3.7a)** the samples that showed no diode like behaviour are shown, whereas, **Figure 3.7b)** shows the samples with a good diode like behaviour. The J-V curves presented are representative**.** Henceforth, when the author mentions the figure of merit values for the solar cells it refers to the average values for each sample. The EQE spectra is shown in **Figure 3.7c)**. From the measurements, the solar cells figure of merit were extracted and the average values as well as their standard deviation are shown in **Table 3.** From the EQE curves, it is possible to extract the J_{SC} employing the following equation [19] :

$$J_{SC} = q \int \phi(\lambda) EQE(\lambda) d\lambda \quad (10)$$

where q, is the electron charge, ϕ is the photon flux.

The reference sample showed power conversion efficiency values of 6.17%, and a V_{OC} of 552 mV. The V_{OC} of the reference sample is being limited by rear interface recombination, as ultrathin CIGS solar cells are known to have a high rear interface recombination [34], [37]. By analysing the J-V curve for this sample (**Figure3.7b)**, we note a slope on the 3rd quadrant. The slope is an indication of shunts, which is confirmed by a dark measurement (**Figure 6.4a**), as the same behaviour is present. The difference in the J_{SC} values from the simulated reference sample (30.3 mA/cm^2) with the measured reference sample,23.23 mA/cm^2, is attributed to electrical losses, namely the high interface recombination which is associated with these devices and other losses which are not accounted by the pure optical model (grain boundaries, bulk recombination, band misalignments, etc.) [37]. There is a 1.86 mA/cm^2 J_{SC} difference between the measured by J-V J_{SC} and the J_{SC} calculated trough EQE, 21.37 mA/cm^2. Such difference is linked with the existing shunts in the reference sample [19]. As only a small area is illuminated when doing the EQE measurement, the generated carriers can diffuse trough shunt paths in the non-illuminated area, lowering the EQE values. The introduction of the passivation layer, Al_2O_3, increases the solar cell figures of merit when comparing with the reference sample and reduces the shunting (**Figure 6.4b**). The J_{SC} value is enhanced by 1.86 mA/cm^2, the V_{OC} by 5 mV and the FF by

5.6 %, resulting in 1.5% enhancement on the efficiency value. The measured J-V J_{SC} enhancement is bigger than the simulated J_{SC} enhancement of 0.85 mA/cm^2. Such difference indicates the electrical effects, not taken in consideration in the optical model, gained by the passivation layer are responsible for the enhancement [37], [38]. However, the V_{OC} enhancement (558 mV vs 553 mV) is rather low for the values reported in the literature [37], [38]. The reason for such small enhancement is the "roll-over" seen in the illuminated J-V curve. Such behaviour is common in devices that have insufficient Na in the CIGS layer. [20], [57]. The presence of Na in a CIGS solar cell is known to enhance its electrical properties, as it increases the free carrier concentration by decreasing the electrically active donors [20], [55]. Although the exact physical mechanism for which it happens is still debated [58], [59]. Due to the blocking properties of Al_2O_3, Na is introduced in the solar cell by a NaF precursor layer, deposited before the CIGS. The optimal NaF thickness for an ultrathin CIGS solar cell has not yet been found. We attribute the insufficient Na in this solar cell to a lower NaF thickness than deposited, the deviation comes from an imprecise control on the NaF evaporation process. Hence, due to insufficient Na this solar cell suffers from low V_{OC} values. Consequently, while a fair comparison would be done with an optimum amount of Na, this study alone shows already an additional complexity of the ultrathin approach: ultrathin CIGS layers are much more sensitive to Na contents that thick CIGS layers [55].

The samples that incorporate the metallic layer shows very diverse results, hence we will start by comparing them in terms of efficiency values. The samples which showed the best optical performance in **Section 3.1** ,Mo/Au/Al_2O_3, Mo/Ag/Al_2O_3, and Mo/Cu/Al_2O_3, after the fabrication show extremely low efficiency values, 1.2 %, 2.4 %, 0.04% respectively. The reasons for such low performance will be discussed further below. The samples Mo/Ta/Al_2O_3, and Mo/Ti/Al_2O_3 have efficiency values (1.22 %, 3.98%) lower than the reference samples. The Mo/Zn/Al_2O_3 sample achieved an efficiency value of 7.13 %, having a 0.38 % enhancement over reference sample. One remarkable samples are the ones that incorporate TiW (Mo/TiW/Al_2O_3 -I and II). They achieved efficiency values of 9.86 % for Mo/TiW/Al_2O_3 – I, and 8.86% for Mo/TiW/Al_2O_3-II, with an increase of 3.69% and 1.96 % respectively over the reference sample.

The illuminated J-V curves for the sample Mo/Cu/Al_2O_3 (**Figure 3.7a**) show that this sample is completely shunted. The shunting can occur due to Cu diffusion to the absorber during its growth, changing the CIGS properties. The worst case, like the one seen here, would be the formation of CIGS Cu-rich which is very conductive [33] hence, easily forming shunts paths. Thus, this sample figures of merit are negligible: a V_{OC} of 2 mV and the J_{SC} being 1.34 mA/cm^2, neither FF nor efficiency values could be extracted from this sample. During the CdS deposition, particles agglomerated at the Mo/AlSiCu/Al_2O_3 sample surface, hence affecting its current transport, as the carriers are not able to be collected by the front contact, as seen in the illuminated J-V curve(**Figure 3.7a**). Therefore, this sample figures of merit are heavily affected by this undesirable effect, having a J_{SC} of 0.47 mA/cm^2, V_{OC} of 404 mV and an efficiency value of only 0.04 %. At this point, the reason why a rear metal would influence the top CdS deposition is unknown and very hard to interpret with no similar results in the literature, however, it is known that Al diffuses even better than Cu in CIGS which could lead to a different CIGS morphology leading to a different CdS chemical bath deposition. The, Mo/Ag/Al_2O_3 (**Figure 3.7b**) sample, has a slope in the 3rd quadrant in the illuminated J-V curve, which could indicate shunting problems, however the dark J-V curve shows no sign of shunting (**Figure 6.4c**). Hence, this sample is being affected by voltage-dependent current collection(VDCC)[18], [37]. VDCC occurs in a device with a low effective diffusion length and neglectable loss in the space charge region [18], [37]. In these conditions a small change in the voltage will change the space charge region affecting the current collection of such devices leading to significant changes in the J_{SC}. We attribute the VDCC to high rear interface recombination present in this solar cell [18], [37]. As such, the sample figures of merits are being very limited by the high rear interface recombination with a V_{OC} value of 304 mV and the J_{SC} of 15.43 mA/cm^2. When the solar cell scribing was done, at Uppsala University, problems arise, resulting in some solar cells within the sample having an lower area than defined, resulting in non-trustful J_{SC} values. Such low figures of merit for this sample is attributed to and uncontrolled Ag diffusion to the absorber, leading to additional defects in the CIGS layer [60], [61]. The sample Mo/Au/Al_2O_3(**Figure3.7a**) has the same behaviour as the Mo/Cu/Al_2O_3 (**Figure 3.7a)**. However the Mo/Au/Al_2O_3 sample is still able to generate photocurrent, with J_{SC} values of 22.19 mA/cm^2. The V_{OC} of this solar cell is extremely low 191 mV, due to shunting present in the solar cell. This resulted, in low FF and efficiency values, of 22.1 % and 1.67 %, respectively. The illuminated J-V curve for the sample

$Mo/Zn/Al_2O_3$ (**Figure3.7b)**, indicates an evidence of shunting, confirmed by the dark J-V curve. A cross-over between the J-V curves is also observed (**Figure 6.4 d**). The cross-over happens due to the selenization of Zn, forming ZnSe, a highly resistive n-type semiconductor, hence a formation of p-n junction occurs [62]. Thus, the charge carriers are deviated from the rear contact to the junction, leading to a J_{SC} value of, 23.63 mA/cm^2. Although, this solar cell is still able to achieve a 0.40 mA/cm^2 enhancement over the reference sample, despite the formation of the ZnSe layer. The shunting present in the sample as well the ZnSe layer, leads to a J_{SC} calculated trough EQE , 19.55 mA/cm^2, being significantly smaller than the one measured trough J-V. The V_{OC} enhancement over the reference sample ,590 mV vs 552 mV is enough for the $Mo/Zn/Al_2O_3$ solar cell to show higher efficiency values, 7.13 vs 6.75 %.The samples, $Mo/Ti/Al_2O_3$ (**Figure3.7a)** and $Mo/Ta/Al_2O_3$(**Figure3.7a)** show the same behaviour as the Mo/Al_2O_3 sample (**Figure3.7a)**, with a roll-over being present in the illuminated J-V curve. The reason for these anomalies is attributed to insufficient Na in these samples. Thus, the roll-over heavily limits the efficiency values of these samples, 3.98 % for $Mo/Ti/Al_2O_3$ and 1.22 % for $Mo/Ta/Al_2O_3$. The sample $Mo/Ta/Al_2O_3$ shows a significant difference between the J_{SC} values with the J_{SC} calculated trough EQE being superior by a total of 5.23 mA/cm^2. Such occurrence is linked with a photocurrent barrier[19]. Since, the EQE measurement only shines in a small area of the solar cell, the current generated by that light is enough to pass the barrier as opposed by current generation during the J-V measurement. For the sample $Mo/Ti/Al_2O_3$, bridges between neighbour solar cells remained, after the scribbing, resulting in a non-trustful J_{SC} value of 28.66 mA/cm^2. The samples $Mo/TiW/Al_2O_3$-I and II, show the highest efficiency value of all solar cells fabricated ,9.86% and 8.13% respectively. Both solar cells, show no shunting problems and have similar V_{OC} values 629 mV and 628 mV respectively and FF values, 61.9 % and 60.0 %, respectively. The high V_{OC} is attributed to the passivation effect of the dielectric layer [37], [38]. However, the difference between the J_{SC} values for these samples, 25.25 mA/cm^2 for $Mo/TiW/Al_2O_3$ -I and 21.56 mA/cm^2 for $Mo/TiW/Al_2O_3$- II is due to the partial peel-off that $Mo/TiW/Al_2O_3$ -II suffered during the CBD process. As such no EQE was measured for this sample.

TiW emerges as the most promising material of the metals used in this work, achieving efficiency values 3.69 % (absolute) higher than the reference sample. Sadly, lack of optimization of the NaF evaporation process jeopardized 3 solar cells (Mo/Al_2O_3, $Mo/Ti/Al_2O_3$ and $Mo/Ta/Al_2O_3$) and caused partial peeling of the TiW. The solar cells with highly reflective materials, had diffusion (, $Mo/Ag/Al_2O_3$) or shunting problems ($Mo/Au/Al_2O_3$ and $Mo/Cu/Al_2O_3$). Thus, an alternative CIGS solar structure that can block such diffusion is off high importance, for further enhancing the CIGS absorption. However, such structure needs to be followed by a CIGS growth with very high control in terms of Na.

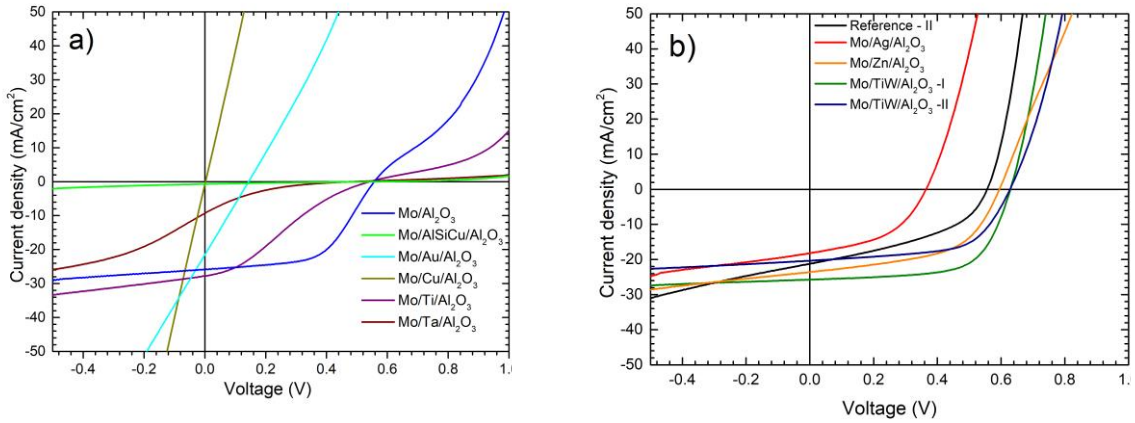

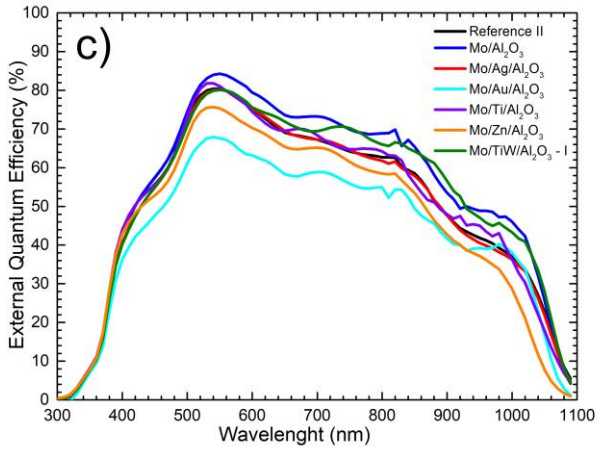

Figure 3.7– Illuminated J-V curves of all the solar cells fabricated: a) Mo/Au/Al2O3, Mo/Cu/Al2O3, Mo/Al2O3 , Mo/Ti/Al2O3, Mo/AlSiCu/Al2O3 and for Mo/Ta/Al2O3; b) for Reference -II,, Mo/Ag/Al2O3, Mo/TiW/Al2O3-I Mo/Zn/Al2O3 and Mo/TiW/Al2O3-II; c) EQE measurements

Table 3 - Average values and standard deviation of the solar cells figure of merit

Sample	V_{OC} [mV]	J_{SC}[mA/cm^2]	EQE J_{SC} [mA/cm^2]	FF[%]	Efficiency[%]
Reference -II	**552 ± 24**	**23.23 ± 1.79**	**21.37 ± 0.32**	**46.6 ± 4.5**	**6.17 ±0.81**
Mo/Al_2O_3	**558 ±23**	**24.68 ± 1.78**	**23.13 ± 0.18**	**55.2 ± 2.5**	**7.67 ±0.72**
Mo/Ag/Al_2O_3	**365 ±13**	**15.43 ± 3.02**	**21.15 ± 0.53**	**49.9 ± 3.0**	**2.84 ± 0.66**
Mo/AlSiCu/Al_2O_3	**404 ±66**	**0.47 ± 0.11**	**N/A**	**21.6 ± 1.2**	**0.04 ± 0.01**
Mo/Au/Al_2O_3	**191 ±77**	**22.19 ± 1.61**	**18.34 ± 1.47**	**26.1 ± 1.7**	**1.21 ± 0.59**
Mo/Cu/Al_2O_3	**2 ± 1**	**1.34 ± 0.30**	**N/A**	**0**	**0**
Mo/Ta/Al_2O_3	**519 ± 41**	**16.12 ± 6.73**	**21.35 ± 4.75**	**14.5 ± 2.0**	**1.22 ± 0.60**
Mo/Ti/Al_2O_3	**532 ± 13**	**28.66 ± 2.57**	**21.29 ± 0.34**	**25.7 ± 1.4**	**3.98 ± 0.50**
Mo/Zn/Al_2O_3	**590 ± 8**	**23.63 ± 1.59**	**19.55 ± 0.41**	**51.1 ± 2.5**	**7.13 ± 0.49**
Mo/TiW/Al_2O_3 - I	**629 ± 6**	**25.25 ± 0.86**	**22.55 ± 0.22**	**61.9 ± 4.5**	**9.86 ± 1.86**
Mo/TiW/Al_2O_3 - II	**628 ± 10**	**21.56 ±1.46**	**N/A**	**60.0 ± 4.5**	**8.13 ± 0.85**

3.4 Alternative CIGS solar cell structure for enhancing light absorption

The fabricated rear solar cell architecture, was not able to prevent the reaction of the metallic layer with the CIGS, due to the contact of the absorber layer with the metal. This reaction proved to degrade the solar cell properties. Thus, a modification of the rear structure to optimize the metal influence is fundamental. In the following section we will present a possible solution. The fabrication

of such structure will be presented as well as the characterization of the samples fabricated employing such structure.

3.4.1 Structure development

In this work, to establish an electrical contact between the CIGS layer and the Mo, **Figure 2.2a)**, the absorber must enter the point-contact. Hence, during the absorber growth, metals can react with CIGS and Se, degrading solar cell properties. One possible solution to prevent such reaction is a deposition of a Mo layer after the etching process, to cover the point-contact and at the same time enabling the formation of an electrical contact to the CIGS. Thus, such structure will be developed with the fabrication steps required to achieve it being described below.

For the implementation of such structure, lift-off process is needed. However, the point-contacts dimensions of 200 nm are not suitable for such process. Hence a new pattern, with wider point-contacts had to be developed. The development of a pattern with a trench configuration was conducted. This pattern is defined by lines with a width of 700 nm, which will be the contact between the CIGS and the Mo. The pitch used on this structure was of 2.8 μm. The exposure made by e-beam would be very time consuming. A lithography system that allows for a lower exposer time was used, a direct writing laser, DWL 2000. The DWL is a high-resolution laser-based optical lithography system with a minimum resolution of 810 nm, for a 415 nm wavelength laser. However, by tuning the intensity and focus of the laser beam the minimum resolution can be lowered to equal the dimension of the features in the pattern (700 nm) The optimized conditions are obtained by the maintenance team at INL. The pattern development produced significant results, resulting in a published scientific paper that can be found in **Annex C**. The second Mo layer deposition has to be done at Uppsala University, as their system provides a more compact layer Mo layer than the deposition system conducted by the Kenosystec at INL.

The initial fabrication steps of this structure are similar to the ones of the structure described in **Section 2.1.** Where 10 nm of a metallic layer are deposited by DC sputtering on top of the rear contact(Mo). The metals used in this series were: Ag,Au,Cu and Ta, they are all deposited using the Kenosistec. Afterwards, 18 nm of Al_2O_3 is deposited on top of the metallic layer, at FTM. The photolithography process starts with the deposition of the positive photoresist AZ1505K with a thickness of 600 nm. After the PR deposition, the samples are then exposed, with a duration of 22 minutes per sample. The samples development is conducted with the developer AZ400K:H_2O 1:4 for 60 seconds. For the opening of the point-contacts RIE is used, with the process taking 45 seconds for all samples. Afterwards, the samples that incorporate the metallic layer are shipped to Uppsala University, for 30 nm deposition of Mo. After the deposition the samples are shipped back to INL for the lift-off process. This process must be done quickly since, the resist AZ1505K ages quickly, making its removal difficult. After, the samples arrival at INL, they are placed in a glass beaker with acetone, with the sample facing tilted to have the surface facing down, and placed in an ultra-sound bath. After, 2 hours of ultrasounds the samples are inspected to verify if the resist was successfully removed, if not, the acetone is changed to remove any particles in the liquid and the samples are left in the ultra-sound bath for another 2 hours. In total, the lift-off process took 8 hours to complete. For the sample Mo/Al_2O_3, a lift-off was not done. Since no metal was deposited on the sample, after the etching process the sample was resist stripped. Due to the initial unavailability of Ag,Au and Cu target at the Kenosistec, the samples Mo/Al_2O_3 and Mo/Ta/Al_2O_3 were fabricated earlier with the remaining samples being fabricated when the targets were available.

The structure of the samples obtained after the lift-off is represented in **Figure 3.8a)** and a schematic showing the fabrication steps in **Figure 3.8b)**.

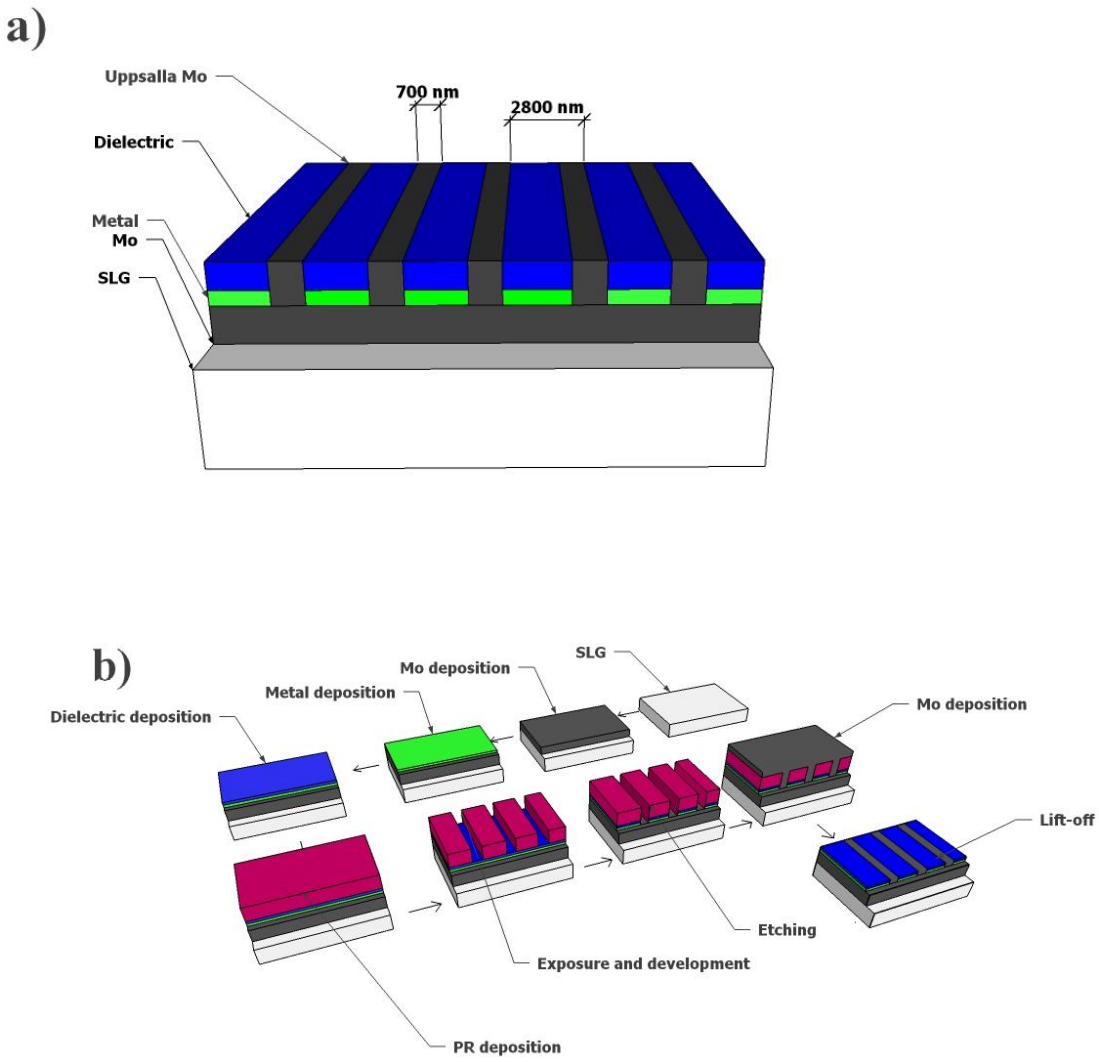

Figure 3.8 - a) representation of the structure obtained after the lift-off; b) Schematic showing the fabrication steps. Both figures are not on scale

In total 6 sets of solar cells were fabricated. One set is a regular CIGS solar cells, designated as reference with a structure: Mo\CIGS\CdS\i:ZnO\Al:ZnO\Ni/Al/Ni grid, another one incorporating only Al_2O_3 with the following structure: Mo\Al_2O_3\CIGS\CdS\i:ZnO\Al:ZnO\Ni/Al/Ni grid. The remaining four sets will use the metal layer, the Al_2O_3 and the Mo layer, with the following structure: Mo\ Metal Al_2O_3\Mo\CIGS\CdS\i:ZnO\Al:ZnO\Ni/Al/Ni grid. The sample names as well the summarized information is found in **Table 4**.

Table 4 - Summarized information of the samples produced with this structure as well as their naming.
Pitch: 2.8 µm; **Line width**:700 nm; **Al_2O_3 thickness**:18 nm; **Metal thickness**: 10 nm

Metal	**Number of samples**	**Sample naming**
Without metal (only Al_2O_3)	1	Mo/Al_2O_3
Au	1	Mo/Au/Al_2O_3/Mo
Ta	1	Mo/Ta/Al_2O_3/Mo
Cu	1	Mo/Cu/Al_2O_3/Mo
Ag	1	Mo/Ag/Al_2O_3/Mo
Reference sample	1	Reference -I

3.4.2 Samples characterization

An analysis of the samples morphology was conducted throughout the fabrication to ensure that the features dimensions were preserved. Hence, in this section, optical microscope images, taken after the samples development and etching process are presented, SEM top-view images were taken after the resist removal for all samples as well as AFM images.

In **Figure 3.9** the morphology of the samples Mo/Al_2O_3 and Mo/Ag/Al_2O_3 are shown, after the development step. The samples have the expected line width (700 nm) as well as the pitch (2.8 µm). We should note that there is still PR on the samples, hence some color changes are observed. For the sample Mo/Ag/Al_2O_3/Mo, a particle is noticed. This particle corresponds to dust in the optical microscope lens and is present for all samples fabricated in that day. Since, Mo/Al_2O_3 and Mo/Ta/Al_2O_3/Mo were fabricated on a different day, the dust is not present. Since, all samples show the same pattern, for simplicity we only show images of these two samples.

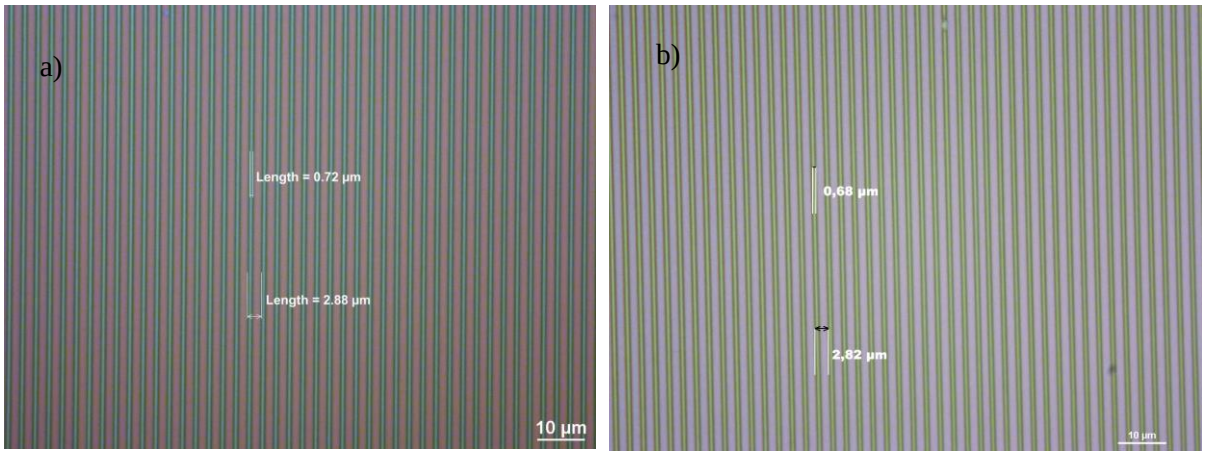

Figure 3.9-Post development optical microscope pictures of samples: Mo/Al2O3 (a) and Mo/Ag/Al2O3/Mo (b). The expected line width (700 nm) is achieved for all the samples as well as the pitch (2.8 µm). A 100X magnification was used.

The etching process did not affect the pattern dimensions as seen in **Figure 3.10**. The samples Mo/Ag/Al_2O_3/Mo and Mo/Cu/Al_2O_3/Mo have particles randomly disposed trough out the trenches. The particles presence might be due to a reaction of metals with the chlorine ions during the etching process, indicating the reactivity of such metals. The samples Mo/Au/Al_2O_3 and Mo/Ta/Al_2O_3/Mo, does not have any particles in their surface. For the sample Mo/Al_2O_3, only SEM pictures were taken after the resist removal.

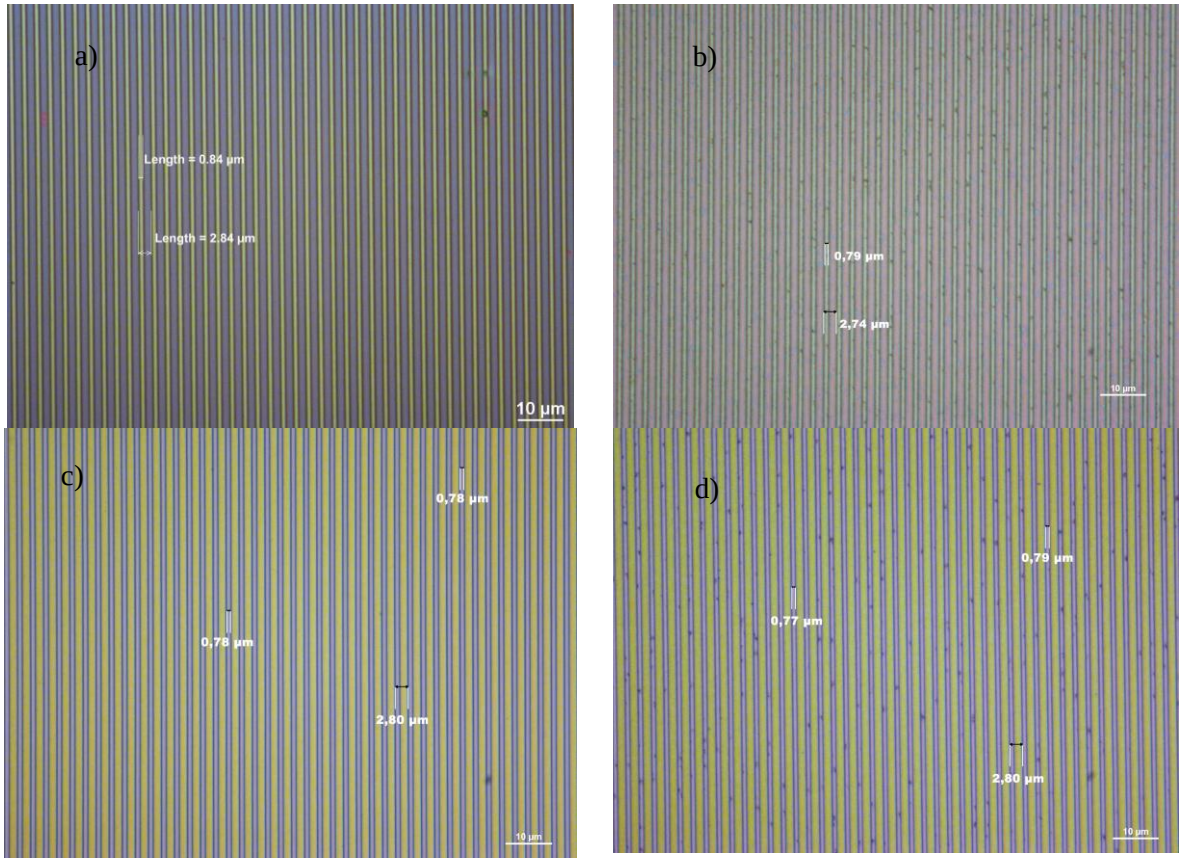

Figure 3.10 - Optical microscope pictures of the samples after the etching; a) Mo/Ta/Al2O3/Mo; b) Mo/Ag/Al2O3/Mo; c) Mo/Au/Al2O3/Mo; d) Mo/Cu/Al2O3/Mo .The lines width and the pitch were preserved. Some particles seem to appear randomly in the samples Mo/Ag/Al2O3/Mo and Mo/Cu/Al_2O_2/Mo

The sample Mo/Cu/Al_2O_3 was shattered when packing at Uppsala University, hence no further processing was done to that sample.

After the Mo deposition and the consequent lift-off process, top-view SEM images were taken for all samples, with the results, being present in **Figure 3.11.** The pictures taken trough SEM confirms the dimensions taken by optical microscope, small deviations in the measurements are due to the high sensibility of the optical microscope when measuring distances. Some reaction occurred with the Al_2O_3 layer in the Mo/Ag/Al_2O_3/Mo sample, **Figure 3.11b**), as it seems that the Al_2O_3 layer was consumed. Nevertheless, the remaining samples have a well-defined pattern after the lift-off, with the Mo grains being visible in the samples Mo/Ag/Al_2O_3/Mo, Mo/Au/Al_2O_3/Mo and Mo/Ta/Al_2O_3/Mo, indicating a conformal deposition. Near the lines edges, some residues of PR are noticed indicating that the photoresist was not removed. After, this observation the samples went to an ultrasound bath with acetone for removing the remaining PR residues, however it was not possible to remove these residues.

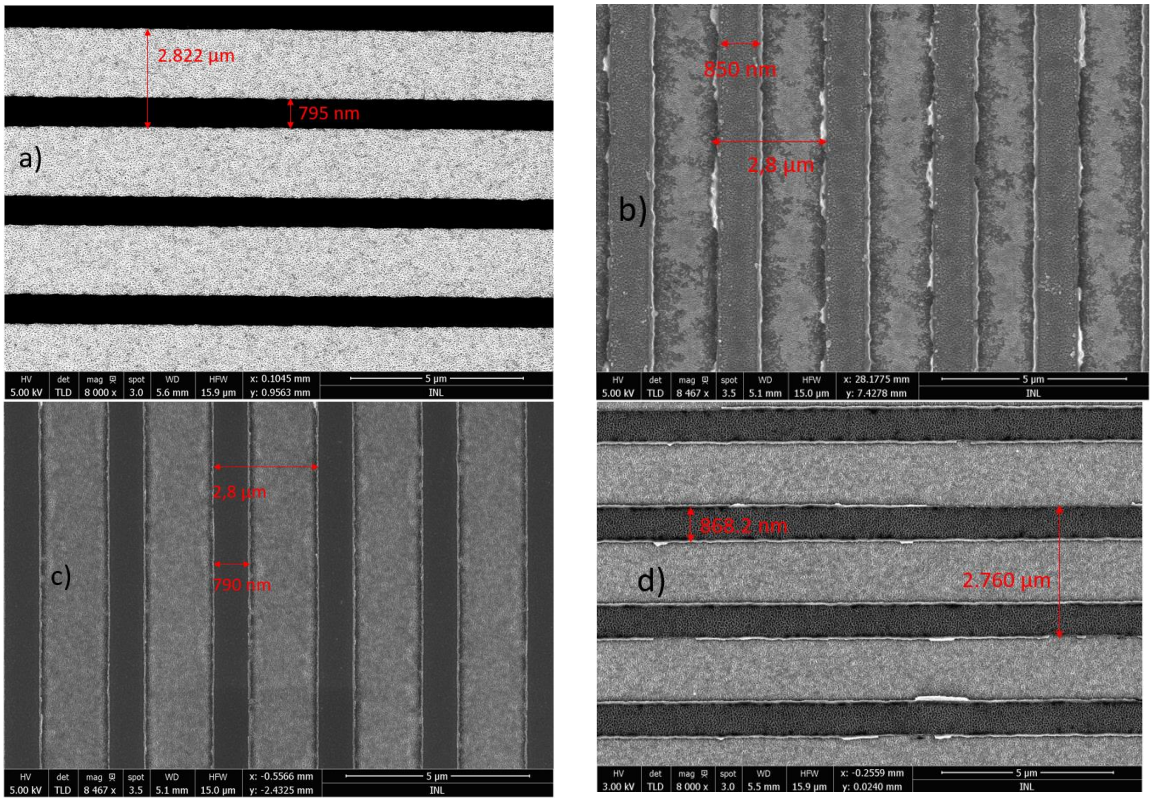

Figure 3.11 - SEM pictures of samples after the lift-off: a)Mo/Al_2O_3 ; b) Mo/Ag/ Al_2O_3/Mo; c) Mo/Au/ Al_2O_3/Mo; d)Mo/Ta/Al_2O_3/Mo

For a better understanding of the samples morphology after the lift-off, AFM analysis was conducted with the results being represented in **Figure 3.12.** The trenches depth can only be analysed in the Mo/Al_2O_3 sample, as in this sample, no Mo deposition was done. **Figure 3.12 a)**, shows a vertical trench with a depth of 42 nm and 700 nm width, thus achieving the desired dimensions. The scan line clearly shows that the Al_2O_3 was fully etched, since the hole depth is 42 nm and the thickness of Al_2O_3 used was 18 nm. The difference is due to an over etch we performed on the Mo layer to ensure that the Al_2O_3 layer is uniformly open through the whole sample. The line width measured by AFM matches the measurement taken in SEM, as seen in **Figure 3.11 a).** The sample Mo/Ta/Al_2O_3/Mo shows sidewalls near the trenches edges. Such sidewalls, with a height of 70 nm, comes from an incomplete lift-off as seen in **Figure 3.11d),** the deposition of the second Mo layer is very conformal; hence it coats the photoresist sidewalls. Thus, when performing a lift-off, the acetone encounters a barrier in the sidewalls of the photoresist, rendering difficult for the liquid to diffuse to the photoresist, hindering the lift-off process. The sidewalls present in the sample, are an indication that: i) a more direct deposition technique should be used to prevent sidewalls; ii) a photoresist who develops an undercut profile should be considered, when a lift-off is desired in the fabrication process. Despite the formation of sidewalls, the trench hole was not fully etched as a lump is seen after the lift-off. This lump indicated that the etching time was not enough to open a trench hole with depth of 30 nm, hence the lump is noticed. The sample Mo/Au/Al_2O_2/Mo also has sidewalls on the trenches edge, roughly 30 nm. The scan line of Mo/Au/Al_2O_2/Mo shows, a trench width of around 800 nm, although the hole depth is nearly the same of the Mo/Al_2O_3 sample. This depth occurred due to Mo not being able to fill the trenches during its deposition, but rather it adhered to the resist sidewalls. Such occurrence could be confirmed by performing cross-section analysis with SEM. However, such analysis had to done after the Mo deposition and since the Mo/Ta/Al_2O_3/Mo did had present such anomalies, a cross-section of the sample was not performed. The surface of the sample Mo/Ag/Al_2O_2/Mo has particles spread randomly throughout the sample. The particle formation has occurred during the etching process due to a reaction of Ag with chorine ions. Such reaction is also responsible for damaging the Al_2O_3 layer, as seen in **Figure 3.12c).**

These samples were shipped to Uppsala University, for full solar cell processing. Unfortunately, they did not arrive in time to be included in this master thesis.

a)

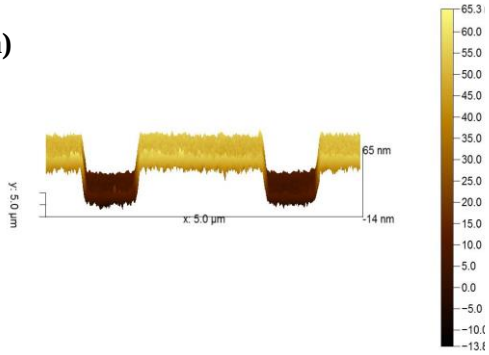

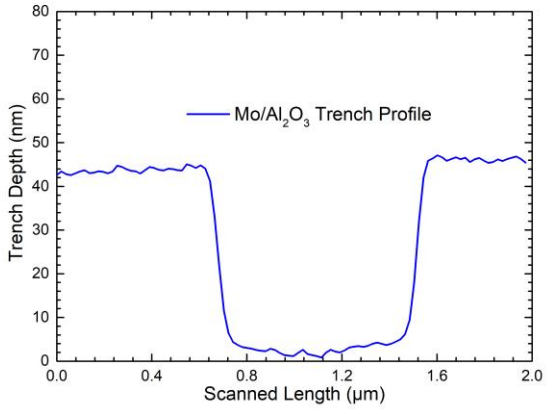

b)

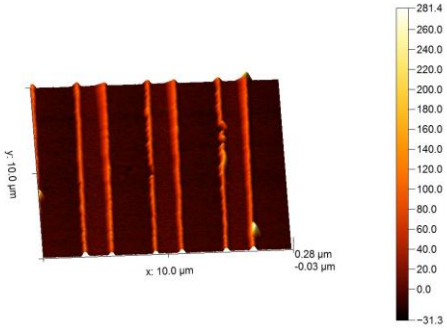

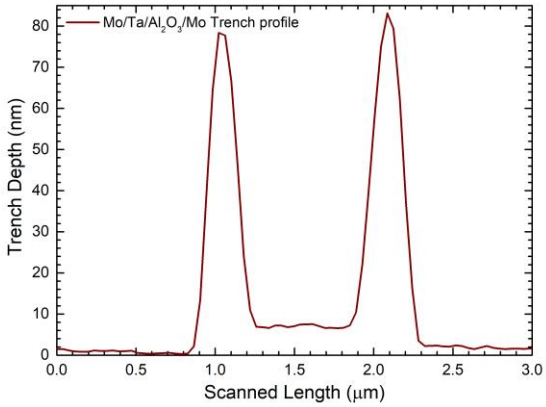

c)

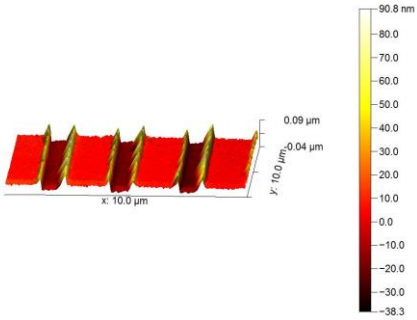

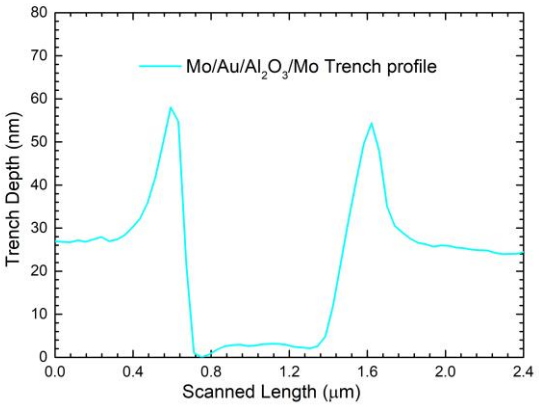

d)

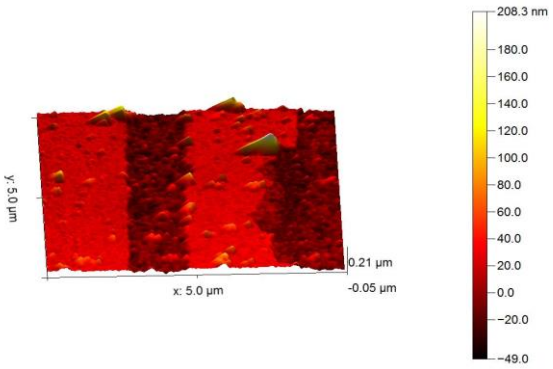

Figure 3-12– AFM images of the samples fabricated. a) Mo/Al2O3, shows a clean surface with a trench depth of 45 nm with a 700 nm trench width; b) Mo/Ta/Al2O3/Mo, shows a clean surface with sidewalls at the trenches edges; c) Mo/Au/Al2O3/Mo, has a clean surface, with sidewalls present in the sample; d) Mo/Ag/Al_2O_3/Mo, particles spread throughout the surface and with Al_2O_3 layer being damaged.

4 Conclusions and future perspectives

The main objective of this master thesis was to enhance the light absorption of an ultrathin CIGS solar cell. As such the rear structure of a CIGS solar cell was modified to include a metal layer, above the rear contact and below the dielectric layer. For the creation of the desired pattern of, a square array of 200 nm holes with a pitch of 2µm, e-beam lithography was used. The dielectric material to function as a passivation layer was Al_2O_3.Six different metals (Ag,Au,Cu,Ta,Ti,Zn) and 2 metallic alloys (AlSiCu and TiW) were tested.

Optical simulations were conducted employing the commercial software *Lumerical*, to study the optical influence of the metals in the solar cell structure. First, to identify the main optical loss of an ultrathin CIGS solar cell, a comparison was done with a regular a 2 µm thick absorber CIGS solar cell. By accounting only optical considerations, the decrease in the CIGS layer thickness is responsible for a loss of 3.53 mA/cm^2 in J_{SC} with 2.4 mA/cm^2 being lost by the rear contact due to its poor reflection, thus indicating the parasitic light absorption at the rear is the main optical loss in an ultrathin CIGS solar cell. Optical simulations with the fabricated solar cells structures showed that all solar cells that had the metallic layer in their constitution showed an enhancement in J_{SC} over the reference solar cell. The solar cells that incorporated the metallic layer of Ag, Cu and Au had the highest enhancement in CIGS light absorption and at the same time decreasing the parasitic light absorption at the rear. Nonetheless, the highest performance solar cell was still not able to achieve J_{SC} values equal to the regular thick CIGS solar cell. Such fact is linked to light, when reflected back by the metal layer, exiting the solar cell rather than being absorbed. As such, for further increasing of CIGS light absorption, light trapping schemes that promote a longer light path must be used

With regards to the fabrication of the simulated substrates, SEM top view images after the resist stripping, showed that the fabrication was successful in creating the desired nanopattern. However, the holes dimensions were elongated in a particular direction due to astigmatism of the e-beam system. Such process was long as INL's cleanroom is optimized for 200 mm diameter 0.7 mm thick silicon wafers and the handling of the 5x5 cm^2 square, 1 mm thick glass substrates was complex and needed different optimization compared with the silicon standards.

After using the novel substrates to fabricate solar cells and when comparing the solar cells results, we note that our reference sample is heavily affected by electrical losses, seen by the low V_{OC} value and by the difference between the simulated and measured $J_{SC,}$ 30.03 mA/cm^2 vs 21.37 mA/cm^2. Such difference is expected as the simulations only accounted for optical losses and in ultrathin devices there is a significant increase in rear recombination at the rear. By simply introducing the passivation layer, an enhancement of the solar cells figures of merit over the reference solar cell is observed. However, this sample suffered from Na deficiency. Such anomaly is also present in samples Mo/Ta/Al_2O_3 and Mo/Ti/Al_2O_3. Several devices had anomalous and worse performances than the reference device. Such behavior is linked with a reaction of the metallic layer with CIGS and Se, such reaction could not be accounted in the optical simulations. Nonetheless, the Mo/TiW/Al_2O_3 achieved significant results, with an increase of 73 mV in V_{OC} and 1.98 mA/cm^2 in J_{SC} resulting in an impressive 3.69 % (absolute) enhancement over the reference sample.

The reaction of the metal with CIGS and Se, jeopardized the samples performance. As such, a modification of the rear structures of a CIGS solar cell to prevent such reaction was proposed. Such solution, passed by a deposition of a second Mo layer, to fill the point contacts and to establish electrical contact with the CIGS. However, to implement this Mo layer, the structure used in our solar cells had to be modified, has the point contacts dimensions achieved through e-beam are too small to conduct a lift-off process. Thus, a trench pattern was developed with a contact line of 700 nm, and a pitch 2.8 µm, utilizing DWL for the lithography process.

Optical microscope and SEM top-view images showed that the expected pattern dimension was achieved and preserved trough out the fabrication steps. AFM analysis confirmed the dimensions obtained, however for the samples that went through the lift-off process sidewalls were noticed. Such sidewalls are due to the uniformity of the Mo deposition as the metal is deposited on the sidewalls of the

photoresist, compromising its removal. The surface of the Mo/Ag/Al_2O_3/Mo/ sample was very damaged, probably due to a reaction of Ag with the chlorine ions during the etching, as indicated by optical microscope images after the etching process, damaging the Al_2O_3 layer. In the end, these samples were shipped to Uppsala University for full solar cell processing and further analysis. These substrates must be improved in terms of lift-off process, either by using a photoresist that develops an undercut profile or by employing non-conformal deposition techniques. Afterwards, solar cells with a precise control over the Na doping needs to be fabricated to evaluate if this concept works.

The next step for this work would be for an optimization of the lift-off process, to prevent sidewalls. This optimization could be done by using a negative resist or by employing a LOR layer before the PR coating, for the creation of an undercut profile. The application of a LOR layer is at a preliminary stage, however due to delays during the process it was not possible to show any preliminary results. Since, the solar cells with a TiW layer showed very promising results, more samples should be fabricated to better comprehend the metal influence on the solar cell properties. The NaF layer deposition and the solar cell definition are processes that needs optimization. As such solar cells should be fabricated, with the purpose of optimize the NaF thickness for ultrathin CIGS solar cells. However, the optimization for these processes can only be done by our collaborators at Uppsala University. Thus, given the anomalies presented by the samples produced in this work, the optimization already began and hopefully it will be a step further at optimizing the solar cells power conversion efficiency.

5 References

[1] D. M. Chapin, C. S. Fuller, and G. L. Pearson, "A New Silicon p-n Junction Photocell for Converting Solar Radiation into Electrical Power," *J. Appl. Phys.*, vol. 25, no. 5, pp. 676–677, May 1954.

[2] K. L. Chopra, P. D. Paulson, and V. Dutta, "Thin-film solar cells: an overview," *Prog. Photovoltaics Res. Appl.*, vol. 12, no. 23, pp. 69–92, 2004.

[3] M. A. Green, "The Passivated Emitter and Rear Cell (PERC): From conception to mass production," *Sol. Energy Mater. Sol. Cells*, vol. 143, pp. 190–197, 2015.

[4] A. Shah, P. Torres, R. Tscharner, N. Wyrsch, and H. Keppner, "Photovoltaic technology: The case for thin-film solar cells," *Science (80-.).*, vol. 285, no. 5428, pp. 692–698, 1999.

[5] S. Siebentritt, "What limits the efficiency of chalcopyrite solar cells?," *Sol. Energy Mater. Sol. Cells*, vol. 95, no. 6, pp. 1471–1476, 2011.

[6] M. A. Green, Y. Hishikawa, E. D. Dunlop, D. H. Levi, J. Hohl-Ebinger, and A. W. Y. Ho-Baillie, "Solar cell efficiency tables (version 51)," *Prog. Photovoltaics Res. Appl.*, vol. 26, no. 1, pp. 3–12, 2018.

[7] "Solar Frontier Achieves World Record Thin-Film Solar Cell Efficiency of 22.9%." [Online]. Available: http://www.solar-frontier.com/eng/news/2017/1220_press.html. [Accessed: 11-Jul-2018].

[8] I. Renewable Energy Agency, "Renewable Energy Cost Analysis: Solar Photovoltaics," 2012.

[9] V. Fthenakis, "Sustainability of photovoltaics: The case for thin-film solar cells."

[10] N. Naghavi *et al.*, "Ultrathin Cu(In,Ga)Se2based solar cells," *Thin Solid Films*, vol. 633, no. October 2017, pp. 55–60, 2017.

[11] G. Yin *et al.*, "Well-controlled dielectric nanomeshes by colloidal nanosphere lithography for optoelectronic enhancement of ultrathin Cu(In,Ga)Se2solar cells," *ACS Appl. Mater. Interfaces*, vol. 8, no. 46, pp. 31646–31652, 2016.

[12] R. J. Matson *et al.*, "Metal contacts to CuInSe2," *Sol. Cells*, vol. 11, no. 3, pp. 301–305, Apr. 1984.

[13] E. Moons, T. Engelhard, and D. Cahen, "Ohmic Contacts to p-CulnSe 2 Crystals," *J. Electron. Mater.*, vol. 22, no. 3, 1993.

[14] K. Orgassa, H. W. Schock, and J. H. Werner, "Alternative back contact materials for thin film Cu(In,Ga)Se2solar cells," *Thin Solid Films*, vol. 431–432, no. 03, pp. 387–391, 2003.

[15] P. M. P. Salomé, "Chalcogenide Thin Films For Solar Cells: Growth and Properties," 2011.

[16] S. M. Sze and K. K. Ng, *Semiconductor Devices: Physics and Technology*. 2006.

[17] "Solar Cell Parameters and Equivalent Circuit 9.1 External solar cell parameters." [Online]. Available: https://ocw.tudelft.nl/wp-content/uploads/solar_energy_section_9_1_9_3.pdf. [Accessed: 11-Jul-2018].

[18] S. S. Hegedus and W. N. Shafarman, "Thin-film solar cells: device measurements and analysis," *Prog. Photovoltaics Res. Appl.*, vol. 12, no. 23, pp. 155–176, 2004.

[19] R. Scheer and H. Schock, *Chalcogenide photovoltaics*. 2011.

[20] P. Salomé, V. Fjällström, A. Hultqvist, and M. Edoff, "Na doping of CIGS solar cells using low sodium-doped mo layer," *IEEE J. Photovoltaics*, vol. 3, no. 1, pp. 509–513, 2013.

[21] J. Lindahl *et al.*, "Inline Cu(In,Ga)Se2 co-evaporation for high-efficiency solar cells and modules," *IEEE J. Photovoltaics*, vol. 3, no. 3, pp. 1100–1105, 2013.

[22] F. Mollica, F. Mollica, C. In, and G. Se, "Optimization of ultra-thin Cu (In , Ga) Se2 based solar cells with alternative back-contacts Optimization of ultra-thin Cu (In , Ga) Se 2 based solar cells with alternative back-contacts Présentée par Fabien MOLLICA," 2017.

[23] B. Sang, Y. Nagoya, K. Kushiya, and O. Yamase, "MOCVD-ZnO windows for 30 cm×30 cm CIGS-based modules," *Sol. Energy Mater. Sol. Cells*, vol. 75, no. 1–2, pp. 179–184, Jan. 2003.

[24] S. Gledhill *et al.*, "A spray pyrolysis route to the undoped ZnO layer of Cu(In,Ga)(S,Se)2 solar cells," *Thin Solid Films*, vol. 517, no. 7, pp. 2309–2311, Feb. 2009.

[25] L. C. Olsen, P. Eschbach, and Sambhu Kundu, “Role of buffer layers in CIS-based solar cells,” in *Conference Record of the Twenty-Ninth IEEE Photovoltaic Specialists Conference, 2002.*, pp. 652–655.
[26] S. Wagner, J. L. Shay, P. Migliorato, and H. M. Kasper, “$CuInSe_2$/CdS heterojunction photovoltaic detectors,” *Appl. Phys. Lett.*, vol. 25, no. 8, pp. 434–435, Oct. 1974.
[27] R. A. Mickelsen, W. S. Chen, Y. R. Hsiao, and V. E. Lowe, “Polycrystalline thin-film $CuInSe_2$/CdZnS solar cells,” *IEEE Trans. Electron Devices*, vol. 31, no. 5, pp. 542–546, May 1984.
[28] A. M. Gabor, J. R. Tuttle, D. S. Albin, M. A. Contreras, R. Noufi, and A. M. Hermann, “High-efficiency $CuIn_xGa_{1-x}Se_2$ solar cells made from $(In_x,Ga_{1-x})_2Se_3$ precursor films,” *Appl. Phys. Lett.*, vol. 65, no. 2, pp. 198–200, Jul. 1994.
[29] D. Abou-Ras *et al.*, “Innovation highway: Breakthrough milestones and key developments in chalcopyrite photovoltaics from a retrospective viewpoint,” *Thin Solid Films*, vol. 633, pp. 2–12, 2017.
[30] “ZSW: ZSW Sets New World Record for Thin-film Solar Cells.” [Online]. Available: https://www.zsw-bw.de/en/newsroom/news/news-detail/news/detail/News/zsw-sets-new-world-record-for-thin-film-solar-cells.html. [Accessed: 11-Jul-2018].
[31] “Hanergy’s Solibro has 20.5% CIGS solar cell verified by NREL | PV Tech.” [Online]. Available: https://www.pv-tech.org/news/hanergys_solibro_has_20.5_cigs_solar_cell_verified_by_NREL. [Accessed: 11-Jul-2018].
[32] University of Delft, “Solar energy,” *Solar energy*. [Online]. Available: https://ocw.tudelft.nl/wp-content/uploads/solar_energy_section_13_4_1.pdf. [Accessed: 11-Jul-2018].
[33] A. Rockett and R. W. Birkmire, “CuInSe 2 for photovoltaic applications,” *Cit. J. Appl. Phys.*, vol. 70, p. 81, 1991.
[34] B. Vermang, V. Fjällström, J. Pettersson, P. Salomé, and M. Edoff, “Development of rear surface passivated Cu(In,Ga)Se2 thin film solar cells with nano-sized local rear point contacts,” *Sol. Energy Mater. Sol. Cells*, vol. 117, pp. 505–511, 2013.
[35] J. Kessler, C. Chityuttakan, J. Lu, J. Schöldström, and L. Stolt, “$Cu(In,Ga)Se_2$ thin films grown with a Cu-poor/rich/poor sequence: growth model and structural considerations,” *Prog. Photovoltaics Res. Appl.*, vol. 11, no. 5, pp. 319–331, Aug. 2003.
[36] T. Dullweber *et al.*, “Study of the effect of gallium grading in Cu(In,Ga)Se2,” *Thin Solid Films*, vol. 361–362, pp. 478–481, Feb. 2000.
[37] P. M. P. Salomé *et al.*, “Passivation of Interfaces in Thin Film Solar Cells: Understanding the Effects of a Nanostructured Rear Point Contact Layer,” *Adv. Mater. Interfaces*, vol. 5, no. 2, pp. 1–10, 2018.
[38] B. Vermang *et al.*, “Employing Si solar cell technology to increase efficiency of ultra-thin Cu(In,Ga)Se2 solar cells.,” *Prog. photovoltaics*, vol. 22, no. 10, pp. 1023–1029, Oct. 2014.
[39] W. Wu *et al.*, “Characterization of CZTSSe photovoltaic device with an atomic layer-deposited passivation layer,” *Appl. Phys. Lett.*, vol. 105, no. 4, p. 042108, Jul. 2014.
[40] Y. Fu *et al.*, “ZnS Nanodot Film as Defect Passivation Layer for Cu(In,Ga)(S,Se)2 Thin-Film Solar Cells Deposited by Spray-ILGAR (Ion-Layer Gas Reaction),” *Adv. Energy Mater.*, vol. 1, no. 4, pp. 561–564, Jul. 2011.
[41] J. M. V. Cunha *et al.*, “Insulator materials for interface passivation of $Cu(In,Ga)Se_2$ thin films,” *IEEE J. Photovoltaics*, pp. 1–6, 2018.
[42] “Lumerical Inc. | Innovative Photonic Design Tools.” [Online]. Available: https://www.lumerical.com/. [Accessed: 30-May-2018].
[43] P. E, “E. Palik-Handbook of Optical Constants of Solids [Vols. 1-4 combined]-AP (1998).pdf.” .
[44] W. S. M. Werner, K. Glantschnig, and C. Ambrosch-Draxl, “Optical Constants and Inelastic Electron-Scattering Data for 17 Elemental Metals,” *J. Phys. Chem. Ref. Data*, vol. 38, no. 4, pp. 1013–1092, Dec. 2009.
[45] “Angstrom Sun Technologies Inc. | NK Material List.” [Online]. Available: http://www.angstec.com/graph/13. [Accessed: 29-May-2018].
[46] P. D. Paulson, R. W. Birkmire, and W. N. Shafarman, “Optical characterization of CuIn1-xGaxSe2 alloy thin films by spectroscopic ellipsometry,” *J. Appl. Phys.*, vol. 94, no. 2, pp. 879–

888, 2003.
[47] M. J. Mendes *et al.*, “Optimal-Enhanced Solar Cell Ultra-thinning with Broadband Nanophotonic Light Capture,” 2018.
[48] M. J. Mendes *et al.*, “Design of optimized wave-optical spheroidal nanostructures for photonic-enhanced solar cells,” *Nano Energy*, vol. 26, pp. 286–296, Aug. 2016.
[49] K. Orgassa, U. Rau, Q. Nguyen, H. Werner Schock, and J. H. Werner, “Role of the CdS buffer layer as an active optical element in Cu(In,Ga)Se2 thin-film solar cells,” *Prog. Photovoltaics Res. Appl.*, vol. 10, no. 7, pp. 457–463, Nov. 2002.
[50] G. Yin, P. Manley, and M. Schmid, “Light trapping in ultrathin CuIn1-xGaxSe2solar cells by dielectric nanoparticles,” *Sol. Energy*, vol. 163, no. October 2017, pp. 443–452, 2018.
[51] G. Yin *et al.*, “Integration of plasmonic Ag nanoparticles as a back reflector in ultra-thin Cu (In, Ga) Se 2 solar cells,” *Appl. Surf. Sci.*, vol. 355, pp. 800–804, 2015.
[52] S. Oueslati *et al.*, “Study of alternative back contacts for thin film $Cu_2ZnSnSe_4$ -based solar cells,” *J. Phys. D. Appl. Phys.*, vol. 48, no. 3, p. 035103, Jan. 2015.
[53] P. Wiklund *et al.*, “A comparison between furnace and rapid thermal annealing (RTA) TiW and Al contacts to shallow p+ junctions,” *J. Phys. Colloq.*, no. C4, p. 49, 1988.
[54] J.-C. Chiou, K.-C. Juang, and M.-C. Chen, “TiW(N) as Diffusion Barriers Between Cu and Si.”
[55] P. M. P. Salomé, H. Rodriguez-Alvarez, and S. Sadewasser, “Incorporation of alkali metals in chalcogenide solar cells,” *Sol. Energy Mater. Sol. Cells*, vol. 143, pp. 9–20, Dec. 2015.
[56] D. Kraft, U. Weiler, Y. Tomm, A. Thissen, A. Klein, and W. Jaegermann, “Alternative back contacts for CdTe solar cells: a photoemission study of the VSe2/CdTe and TiSe2/CdTe interface formation,” *Thin Solid Films*, vol. 431–432, pp. 382–386, May 2003.
[57] R. Caballero *et al.*, “Influence of Na on Cu(In,Ga)Se2 solar cells grown on polyimide substrates at low temperature: Impact on the Cu(In,Ga)Se2/Mo interface,” *Appl. Phys. Lett.*, vol. 96, no. 9, p. 092104, Mar. 2010.
[58] L. E. Oikkonen, M. G. Ganchenkova, A. P. Seitsonen, and R. M. Nieminen, “Effect of sodium incorporation into $CuInSe_2$ from first principles,” *J. Appl. Phys.*, vol. 114, no. 8, p. 083503, Aug. 2013.
[59] E. S. Mungan, X. Wang, and M. A. Alam, “Modeling the Effects of Na Incorporation on CIGS Solar Cells,” *IEEE J. Photovoltaics*, vol. 3, no. 1, pp. 451–456, Jan. 2013.
[60] M. Edoff *et al.*, “High V_{oc} in (Cu,Ag)(In,Ga)Se_2 Solar Cells,” *IEEE J. Photovoltaics*, vol. 7, no. 6, pp. 1789–1794, Nov. 2017.
[61] P. Erslev, G. M. Hanket, W. N. Shafarman, and D. J. Cohen, “Characterizing the effects of silver alloying in chalcopyrite CIGS with junction capacitance methods,” *MRS Proc.*, vol. 1165, pp. 1165-M01-07, Jan. 2009.
[62] J. Timo Wätjen, J. Engman, M. Edoff, and C. Platzer-Björkman, “Direct evidence of current blocking by ZnSe in $Cu_2ZnSnSe_4$ solar cells,” *Appl. Phys. Lett.*, vol. 100, no. 17, p. 173510, Apr. 2012.
[63] J.Tauc, R.Grigorovici, A.Vancu, " Optical Properties and Electronic Structure of Amorphous Germanium, " *Physica status solidi (b)"*, vol 15,pp 627-637, 1996

6 Annexes

6.1 Annex A: CIGS bandgap determination

Tauc et all, develop a method for determining the bandgap using optical absorbance data plotted with respect to energy. It showed that the optical absorption depends on the difference between the photon energy and the bandgap as follows:

$$(\alpha hv)^{1/n} = A(hv - Eg) \tag{11}$$

Where *h* is Planck's constant, *v* is the photon's frequency, α is the absorption coefficient and A is a proportionality constant. The exponent value denotes the nature of electronic transition and since CIGS possesses a direct bandgap, the n takes a value of ½. Trough ref, where the optical constants of CIGS were taken, it is possible to calculate the absorption coefficient, employing the following equation:

$$\alpha = \frac{4\pi k}{\lambda} \tag{12}$$

Where λ is the wavelength and k is the extinction coefficient.

After the calculation of α, we plot the absorption coefficient time the photon energy to the second power $(\alpha hv)^2$versus the incident photon energy (hv) the resulting plot is represented on **Figure 4.1**. The linear region was used to extrapolate to the X-axis to find the bandgap value. The determined bandgap of CIGS with [Ga]/[Ga] + [In] = 0.30is 1.20 eV.

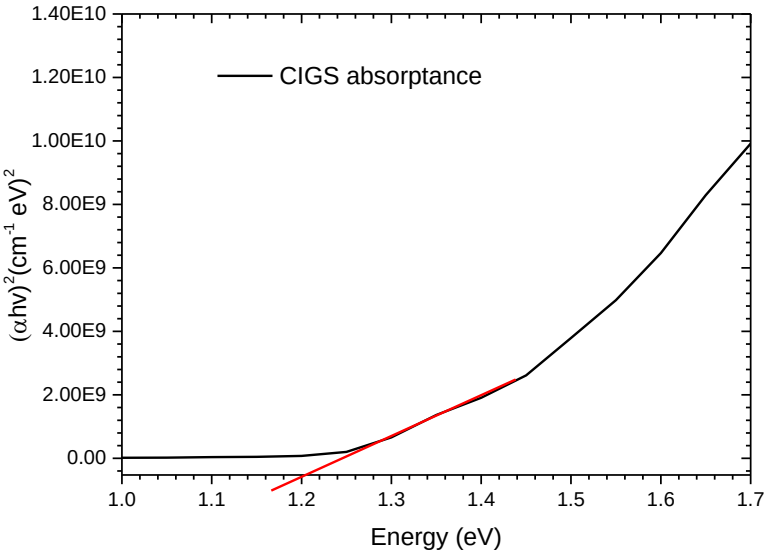

Figure 6.1 Tauc plot analsys of a CIGS layer, with [Ga]/[Ga] + [In] = 0.30. A bandgap of 1.20 eV was determined.

6.2 Annex B:Supplementary figures

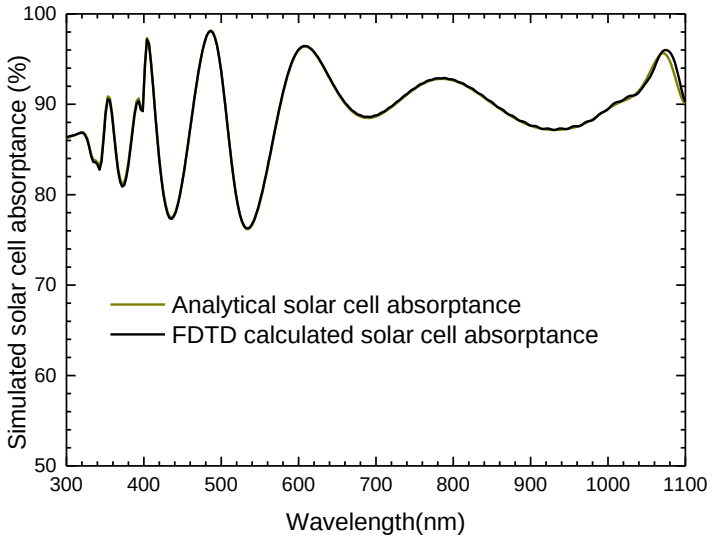

Figure 6.2 Comparison between the Transfer Matrix analytical formalism and the FDTD result, both curves are of the regular CIGS solar cell.

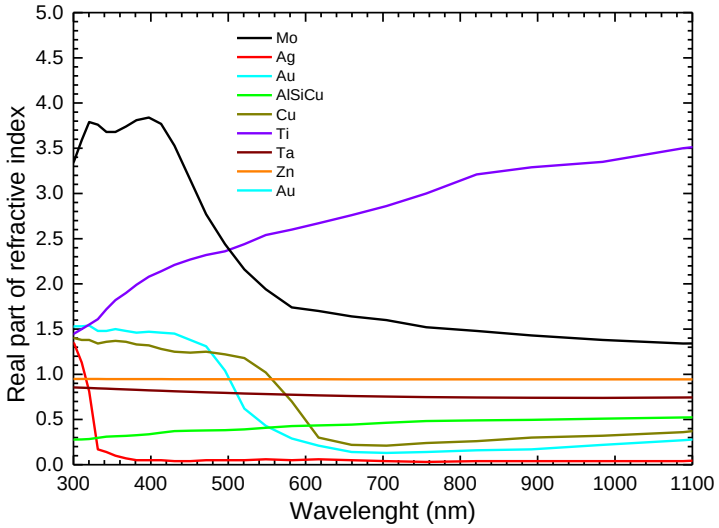

Figure 6.3 - Refractive index of the materials used in the optical simulations

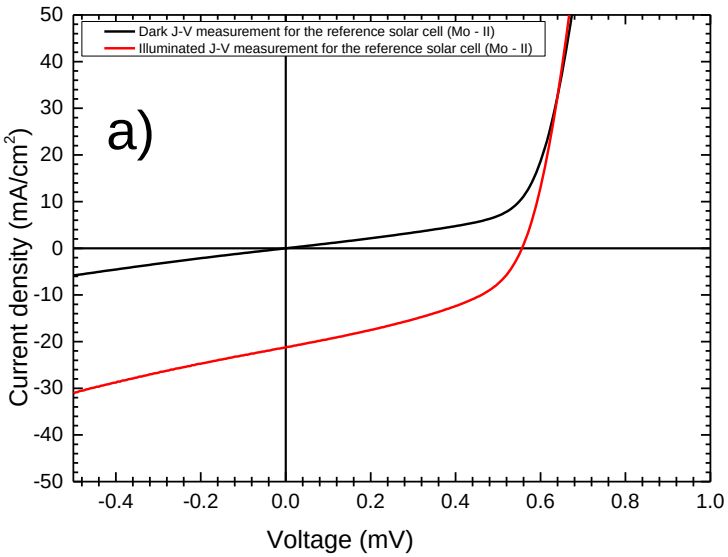
Dark J-V measurement for the reference solar cell (Mo - II)
Illuminated J-V measurement for the reference solar cell (Mo - II)
a)
Current density (mA/cm^2)
Voltage (mV)
50
40
30
20
10
0
-10
-20
-30
-40
-50
-0.4
-0.2
0.0
0.2
0.4
0.6
0.8
1.0

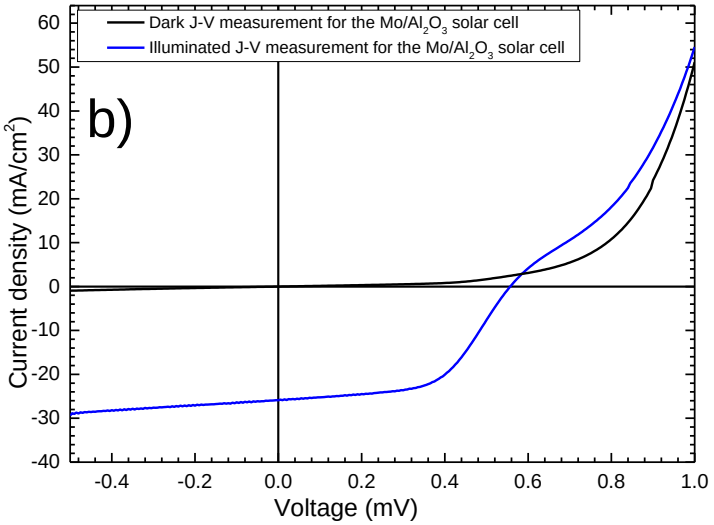
Dark J-V measurement for the Mo/Al$_2$O$_3$ solar cell
Illuminated J-V measurement for the Mo/Al$_2$O$_3$ solar cell
b)
Current density (mA/cm^2)
Voltage (mV)
60
50
40
30
20
10
0
-10
-20
-30
-40
-0.4
-0.2
0.0
0.2
0.4
0.6
0.8
1.0

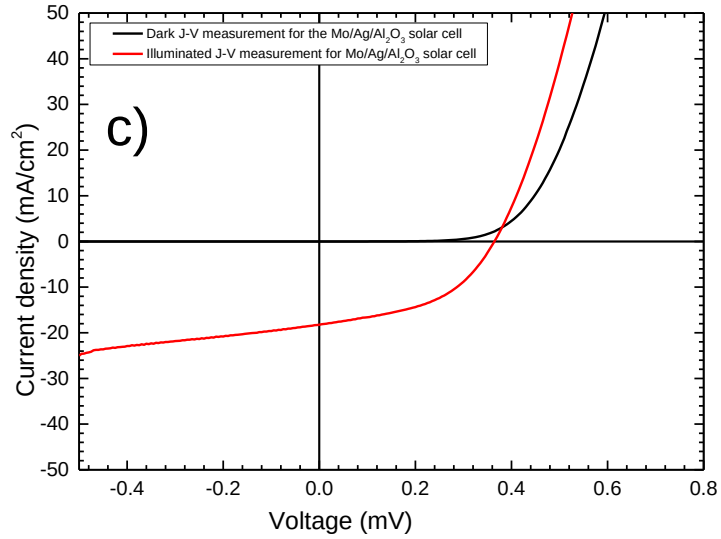

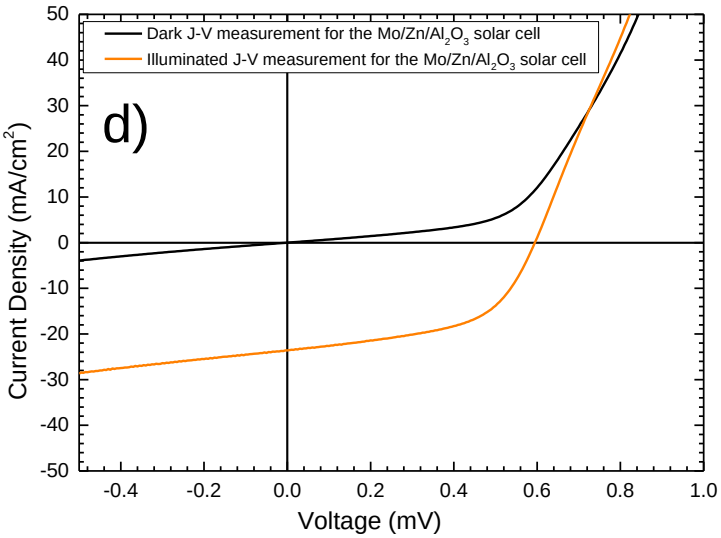

Figure 6.4 - Dark and Illuminated J-V curves for the samples: a) Mo; b)Mo/Al2O3;c)Mo/Ag/Al2O3;d)Mo/Ta/Al2O3

6.3 Annex C: Journal publication

S. Bose, *et al.*, "Optical Lithography patterning of SiO2 layers for interface passivation of thin film solar cells," *Sol. RRL*, 2018.

Keywords: Thin film solar cells; Cu(In,Ga)Se_2 (CIGS); defects passivation; semiconductors; optoelectronics

Abstract: Ultrathin Cu(In,Ga)Se_2 solar cells are a promising way to reduce costs and to increase the electrical performance of thin film solar cells. In this work, we develop an optical lithography process that can produce sub-micrometer contacts in a SiO_2 passivation layer at the CIGS rear contact. Furthermore, an optimization of the patterning dimensions reveals constrains over the features sizes. High passivation areas of the rear contact are needed to passivate the CIGS interface so that high performing solar cells can be obtained. However, these dimensions should not be achieved by using long distances between the contacts as they lead to poor electrical performance due to poor carrier extraction. This study expands the choice of passivation materials already known for ultrathin solar cells and its fabrication techniques.

$Cu(In,Ga)Se_2$ solar cells have reached impressive values of power conversion efficiency, close to 23 %, with the introduction of a post-deposition treatment based in the introduction of alkali-metals that lower front interface recombination.[1–3] By showing that the CIGS interfaces can improve significantly, passivation strategies also for the rear electrode have gained interest. It has been shown that a nanostructured Al_2O_3 layer with point-contacts can lead to significant increase in the efficiency of ultrathin devices by reduction of rear interface recombination.[4–10] It has been demonstrated that due to low CIGS carrier lifetime values, the point contacts need to be separated by distances on the order of magnitude of the diffusion length (500-2000 nm),[4,8–14] meaning that for a passivation area higher than 95 %, contacts with dimensions of one order of magnitude lower (50-200 nm) are needed. Hence, in previous studies, where the passivation effect has been demonstrated, the nanopatterning was made using e-beam lithography by creating a square array of contact circles.[6,9,10] Attempts to use optical lithography have been reported that include the use of etched lines, or trenches, in an Al_2O_3 layer with a width of 3 μm and pitches varying from 6 to 30 μm.[15] In this work, we expand the study of using photolithography to create a patterned insulator layer with etched features with 700 nm and 1400 nm which allow to increase the total passivation area while keeping the distance between the contacts the same order of magnitude as the carrier's diffusion length. Furthermore, according to recent studies indicating that SiO_2 is a promising passivation material, we choose to work with that dielectric material.[16–21]

In this work, we study rear passivation effects on ultrathin CIGS solar cells. This passivation is performed by applying a SiO_2 layer, in a trench configuration, on top of the rear-contact electrode (Mo).[22]

Atomic force microscope (AFM) is used in tapping mode with a scan rate of 1 Hz. J-V measurements are performed under a simulated and calibrated AM1.5 spectra (Oriel Instruments - PVIV Test Solution). External quantum efficiency (EQE) is measured using a QEX10, with a

monochromatic light scanned trough the wavelength interval of 300 nm to 1100 nm with a step of 10 nm. Solar cell cross section images were taken with a Fei-NovaNanoSEM 650 high-resolution scanning electron microscope (SEM), with an acceleration voltage of 3 and 5 kV.

The SiO_2 layers are deposited using a SPTS CVD tool, with a 25 nm thickness on top of the Mo layer at a temperature of 300 ^oC. Prior to the photolithography process, the samples are coated with photoresist AZ1505 with a thickness of 600 nm. The exposure is done using a Direct Write Laser Lithography (DWL 2000) with a 405 nm laser line using a focus setting of 50 and an intensity of 60 % of the total laser output. The used pattern had dimensions of 40000 x 40000 μm and the exposures took around 20 minutes. Afterwards, the sample is developed for 60 seconds, using the developer AZ400K:H_2O 1:4. Afterwards, a physical etching process is performed through the dielectric exposing Mo, allowing for contact of the rear electrode to the CIGS. For this purpose, a reactive ion etching (RIE) process on SPTS ICP is used which according to our experience, does not change the contact properties of the Mo with CIGS.[23] The system is capable of etching deep sub-micron features with near vertical sidewalls (anisotropic) and provides good selectivity. Helium gas is used for aiding backside cooling of the substrate. Ar, BCl_3 and Cl_2 are introduced into the main chamber. 3000KW & 13.56MHz RF Power Supply is used on the source generator achieving a selectivity of 0.4:1 of Al_2O_3 to AZ1505. Finally, to remove the remaining resist, the samples are dipped in acetone and put to ultrasound for 20 minutes. After that, the procedure is repeated using deionized water for 5 minutes.

Figure 5 shows a summary of the trenches fabrication steps used in this work and a schematic of the layers and the structures fabricated for the implementation of the rear contact passivation.

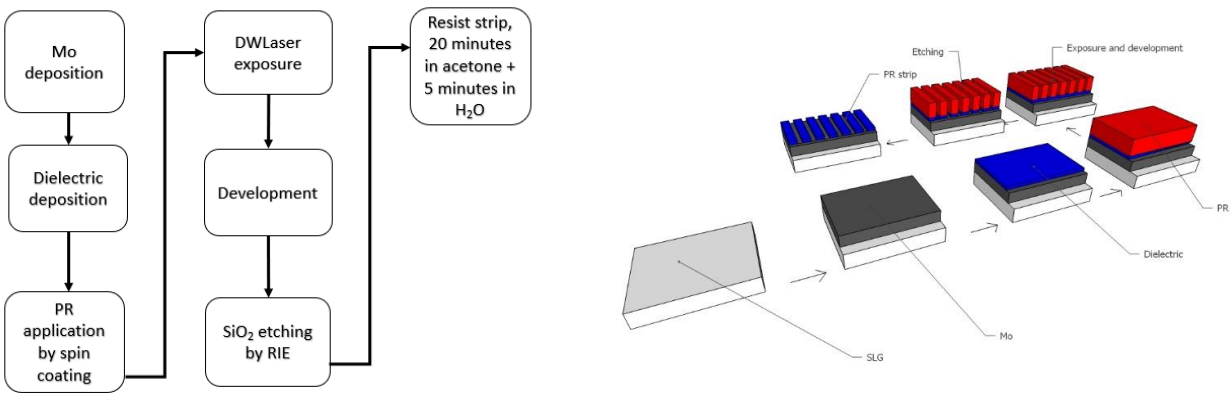

Figure 5 – **Description of the fabrication process of the passivation layer.**

Six sets of samples were fabricated. Each sample had a specific pattern and had 32 cells fabricated. The first set is a reference solar cell with the regular CIGS solar cell structure, SLG/Mo/CIGS/CdS/i-ZnO/ZnO:Al/Ni/Al/Ni grid. On all the other samples, SiO_2 was implemented as passivation layer, with the following structure: SLG/Mo/SiO_2/CIGS/CdS/i-ZnO/ZnO:Al/Ni/Al/Ni grid. The solar cell processing is explained in detail elsewhere [24] and for the CIGS, the layer was co-evaporated at 520 ºC resulting in a thickness of 450 nm and composition [Cu]/([Ga]+[In])=0.7, [Ga]/([Ga]+[In])=0.3 as measured by X-ray fluorescence. Na was introduced as a NaF precursor layer with 10 nm. For the passivation sets, a trench configuration was implemented with line widths of 700 nm and 1400 nm, with variable pitch distances of 2, 4 and 8 μm. The pitch is defined as the inter-distance between the start of two consecutive lines, as shown in **Figure 6**.

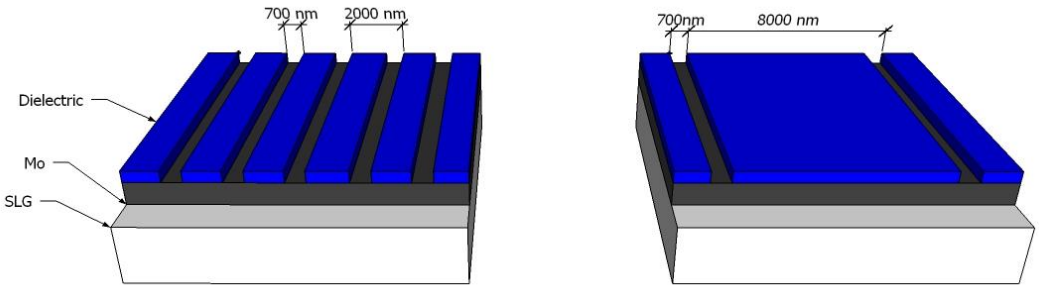

Figure 6 - **Schematic showing some of the structures used: on the left sample H0.7Pitch2 and on the right sample H0.7Pitch8.**

Summarized information is found in **Table 5** where the values of the contact and passivation area are also shown. With regards to the reference sample, we note that the substrates that were used as references were from the same Mo batch and that these substrates were moved between processing together with the patterned substrates to ensure a fair comparison.[25]

Table 5 - **Summary of the samples produced in this work as well the exposure details. The sample naming follows the convention "Hx.x" for hole dimension, "Pitch" for the distance between holes with dimensions given in micrometers.**

Sample name	Exposure details		
	Line Width (µm)	Pitch (µm)	Contact area (%)
H0.7Pitch2	0.7	2	35
H0.7Pitch4	0.7	4	17.5
H1.4Pitch4	1.4	4	35
H0.7Pitch8	0.7	8	8.75
H1.4Pitch8	1.4	8	17.5
Reference	No passivation layer		

As sub-micrometer features can be challenging to be fabricated using standard photolithography processes, a study of the substrate preparation is needed. Hence, AFM was used to investigate if the desired pattern is produced, as shown in **Figure 7** a) and b). All of the substrates showed precise well-defined trenches, however, here we only report on the results of a single pattern for simplicity reasons. The analysis shows a trench that is quite vertical with dimensions similar to the desired ones as expected since the RIE etching process we use provides quite vertical structures and has been optimized for these substrates. The line scan clearly shows that the SiO_2 layer was fully etched, i.e. Mo is exposed, as the hole has a depth of ~ 37 nm and the SiO_2 etched layer has a thickness of 25 nm, as showed in **Figure 7** c). The thickness difference is due to over-etching of the Mo, which we performed to ensure that the SiO_2 layer is uniformly open through the whole sample. A sub-micrometer opening of the SiO_2 layer is achieved, hence, the desired objective of having sub-micrometer openings performed by photolithography was accomplished.

Next, we performed SEM cross-section images of the complete solar cells to analyze if the SiO_2 layer located at the rear would significantly influence the morphology of the CIGS layer and to evaluate film adhesion. This analysis is also important to verify if the passivation layer survives the harsh CIGS growth

conditions

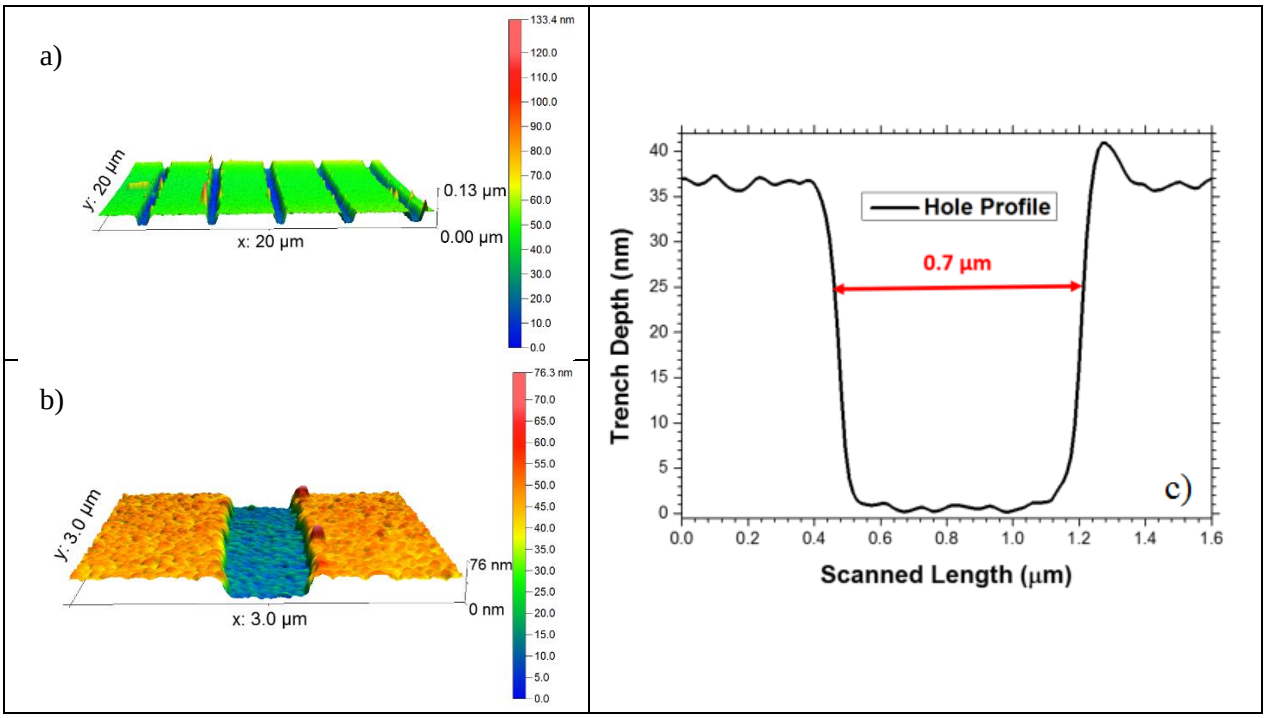

Figure 7 - **AFM analysis of SLG/Mo/SiO_2 substrate. Both a) and b) show a 3D representation of sample H0.7Pitch2 and c) a depth line scan.**

The reference solar cell and two samples, H0.7Pitch2 and H0.7Pitch8 were analyzed and the resulting images are shown in **Figure 8**. The SiO_2 layer, with 25 nm, is challenging to observe due to its thin thickness and its insulating properties, however, in **Figure 8** b) and c), dark layer is observed in between the Mo and the CIGS layer. In fact, in the case of the **Figure 8** c), a hole is present at the left part of the image (highlighted by a circle). These images show that the SiO_2 layer survives the harsh CIGS growth conditions and that there are no adhesion problems. Furthermore, all the samples show the same CIGS morphology with similar grain size, indicating that the SiO_2 layer did not make significant changes to the CIGS structure.

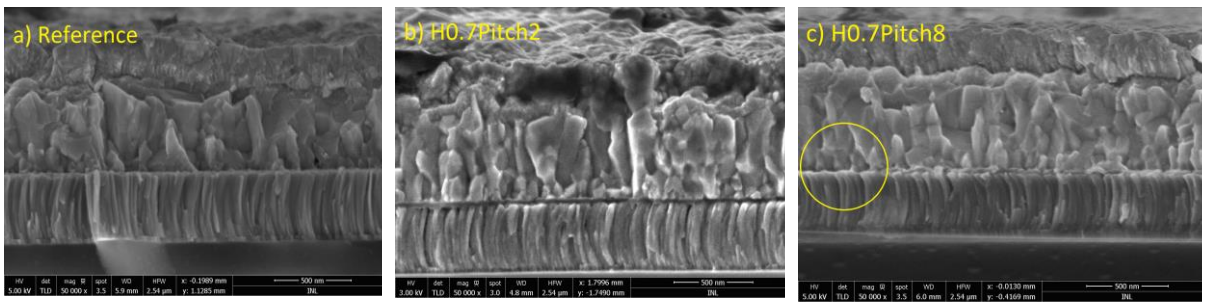

Figure 8 - **SEM cross-section images of the following complete solar cells: a) reference, b) H0.7Pitch2 and c) H0.7Pitch8. The circular area of c) represents an opening in the SiO_2 layer.**

Having shown that sub-micrometer features could be prepared with the desired specifications and that these substrates survive the CIGS growth process, we measured the J-V and EQE behavior of the resulting cells. Representative curves are shown in **Figure 9** and average and standard deviations values of the solar cell figures of merit are shown in **Table 6**. We note that the presented J_{sc} values are corrected with the EQE behavior using the AM1.5 spectra to obtain correct J_{sc} values which is a procedure usually needed in ultrathin devices. Hence, a small mismatch between the J-V representative curves and the EQE representative curves might exist. First, we note that this CIGS run has average quality as the reference device only achieves a power conversion efficiency value of 5 % and this cell suffers from shunting and series resistance as seen in the J-V plot. The reasons for this poor performance might be due to the low GGI composition, the use of a non-optimized alkali concentration, etc. If we only evaluate efficiency, then we notice that there are three passivation patterns that provide cells with an increase in efficiency of almost 1 % (abs.) compared with the reference devices. What is common to these three patterns is that its pitch distance is 2 and 4 μm. We note that sample H0.7Pitch4 has a slightly high V_{oc} and low J_{sc} value, which might be due to a small difference in the composition (GGI) and thickness values, however, the values are still close enough to be comparable. Nonetheless, we can gather the samples in two groups, the first group is where the samples both have an efficiency and a value of V_{oc} * FF higher than the reference one. These samples, H0.7Pitch2, H0.7Pitch4 and H1.4Pitch4, show the typical effects of rear passivation by showing a moderate improvement in V_{oc}, a small improvement in J_{sc} and similar values of FF as the reference devices.[6,8,17,19] Hence, the hypothesis that SiO_2 could be used as a passivation material in CIGS is confirmed. The second group of samples with H0.7Pitch8 and H1.4Pitch8, are the ones where the pattern has a pitch of 8 μm between the SiO_2 openings. These samples show significant problems in carrier extraction as seen by its low values of FF and V_{oc} * FF, which results in efficiency values lower than the ones of the reference device. Such low values are indications of a high contact resistance of the rear electrode. The high contact resistance can be explained by hole accumulation in the rear interface and large values of current density in the small contacts that can lead to Auger recombination with negative impact in the solar cell performance.[26] With regards to the passivation effect, we can focus on samples with the same pitch, so that the contact resistance is comparable, H0.7Pitch4 (580 mV) versus H1.4Pitch4 (521 mV) and H0.7Pitch8 (518 mV) versus

H1.4Pitch8 (400 mV). Here, for the patterns with the same pitch, it is demonstrated that the pattern with the smaller trench dimension (i.e. the pattern with the highest passivation area) always shows the highest values of V_{oc}, a good indication that the rear recombination still has an effect. These results show that there are two effects that influence the electrical behavior of these solar cells. The first effect is connected with the pitch distance and in this experiment it is the dominant effect. If the pitch is too large, it will lead to high values of contact resistance resulting in a degradation of the solar cell performance. The second effect is the rear recombination, for the same pitch distance, high values of passivated area provide cells with better performance. A method to estimate contact resistance between these layers, like transmission line measurement (TLM), would be needed to extract definitive conclusions on the contact properties.

Furthermore, all of the passivated solar cells show a higher optical reflection in the long wavelength regime of the EQE behavior and also an increased J_{sc}. From modelling results it is known that the passivation of the rear interface leads to some increases in V_{oc} and to moderate increases in J_{sc}.[4,8,10] Henceforward, part of the J_{sc} increase can be explained from the passivation effects of the SiO_2 layer. However, the increased reflection of the devices is from light that is not absorbed by the CIGS, is reflected at the Mo/SiO_2, and exits the solar cell. Hence, the introduction of the SiO_2 layer changes the rear reflection but compared with the reference some light still exits the solar cell. Light trapping is then needed to take advantage of the rear increased optical reflection, in good agreement with other studies.[17,19–21,27–30] From these simple measurements, it is hard to find a quantification on the increase of the J_{sc} between the increase in the reflection and the passivation effect.

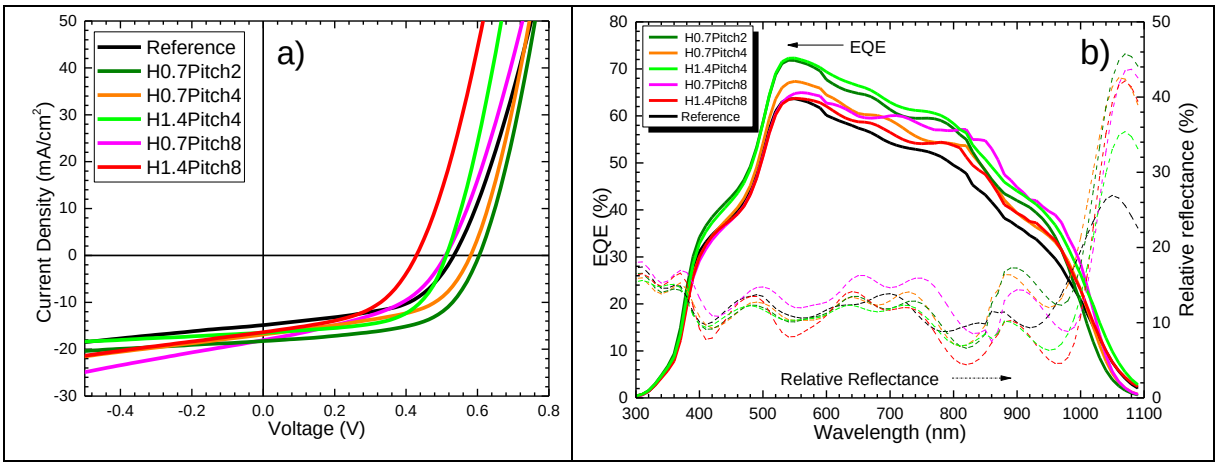

Figure 9 - **a) J-V and b) EQE representative curves of a reference and of rear passivated solar cells. Figure b) also shows the reflectance relative to a $BaSO_4$ reference.**

Table 6 - Average and standard deviations of 32 cells. The figure of merit Voc*FF, ideality factor, G_{shunt} and R_{series} are also presented.

	Graph colour code	J_{sc} EQE (mA/cm²)	V_{oc} (mV)	FF (%)	Eff. (%)	V_{oc} * FF (mV)	Ideality Factor	G_{shunt} (mS.cm^{-2})	R_{series} (Ohm.cm²)
H0.7Pitch2		18.22 ± 0.31	607 ± 5	52.2 ± 8.9	5.77 ± 0.99	315	2.4	1.88 ± 0.46	1.5±0.1
H0.7Pitch4		16.96 ± 0.39	580 ± 1	59.3 ± 4.2	5.84 ± 0.50	342	2.2	2.63 ± 1.67	1.4±0.2
H1.4Pitch4		18.73 ± 0.55	521 ± 30	59.1 ± 4.2	5.77 ± 0.58	307	2.0	2.20 ± 1.31	1.0±0.3
H0.7Pitch8		17.72 ± 1.09	518 ± 16	46.3 ± 6.1	4.28 ± 0.79	240	3.4	12.66 ± 13.04	2.6±0.7
H1.4Pitch8		16.81 ± 1.38	400 ± 23	42.0 ± 3.6	2.83 ± 0.44	168	3	7.34 ± 1.99	3.3±1.0
Reference		16.60 ± 0.94	536 ± 16	55.2 ± 3.4	4.93 ± 0.57	294	2.3	2.75 ± 0.58	1.7±0.5

In this paper we have shown that SiO_2 is a material that passivates the CIGS rear interface of ultrathin solar cells with gains in power conversion efficiency of 1 % (abs.) compared with reference devices. This study expands the choice of passivation materials already known [22,31] and its fabrication techniques. The most important conclusion from this paper is that for flat-Ga ultrathin CIGS solar cells, the pattern of the contacts on the passivation layer is quite important since two competing effects take place. On one hand, low values of contact area are needed to increase the effect of passivation, however, these values must not be made with large electrode distances as these increase contact resistance and lead to low FF and V_{oc} values. Hence, a passivation pattern that has very low contact areas that keeps its electrodes separated at sub-micrometer distances would be ideal.

We have shown that conventional lithography can be used for the creation of a passivation layer that leads to solar cells with power conversion efficiency values higher than reference devices, however, these patterns are likely not optimal and the use of this industrial-friendly technique needs to be optimized in future works. Furthermore, the SiO_2 layer itself can be optimized in terms of fixed electrical charge and thickness, important parameters for interface passivation.

Acknowledgements

Pedro M. P. Salomé acknowledges the funding of Fundação para a Ciência e a Tecnologia (FCT) through the project IF/00133/2015. José M. V. Cunha acknowledges the funding of Fundação para a Ciência e a Tecnologia (FCT) through the project PD/BD/142780/2018. Bart

Vermang has received funding from the European Research Council (ERC) under the European Union's Horizon 2020 research and innovation programme (grant agreement no. 715027). The European Union's Horizon 2020 research and innovation programme ARCIGS-M project (grant agreement no. 720887) is acknowledged. This research is also supported by Development of novel Ultrathin solar cell architectures for low-light, low-cost and flexible opto-electronic devices project (028075) co-funded by FCT and the ERDF through COMPETE2020.
Sourav Bose and José M. V. Cunha contributed equally to this work.

References

1 E. Avancini, R. Carron, T. P. Weiss, C. Andres, M. Bürki, C. Schreiner, R. Figi, Y. E. Romanyuk, S. Buecheler and A. N. Tiwari, *Chem. Mater.*, 2017, **29**, 9695.

2 T. Feurer, P. Reinhard, E. Avancini, B. Bissig, J. Löckinger, P. Fuchs, R. Carron, T. P. Weiss, J. Perrenoud, S. Stutterheim, S. Buecheler and A. N. Tiwari, *Prog. Photovoltaics Res. Appl.*, 2017, **25**, 645.

3 P. Jackson, R. Wuerz, D. Hariskos, E. Lotter, W. Witte and M. Powalla, *Phys. status solidi – Rapid Res. Lett.*, 2016, **10**, 583.

4 B. Vermang, J. T. Watjen, C. Frisk, V. Fjallstrom, F. Rostvall, M. Edoff, P. Salome, J. Borme, N. Nicoara and S. Sadewasser, *IEEE J. Photovoltaics*, 2014, **4**, 1644.

5 B. Vermang, V. Fjallström, X. Gao and M. Edoff, *IEEE J. Photovoltaics*, 2014, **4**, 486–492.

6 P. M. P. Salomé, B. Vermang, R. Ribeiro-Andrade, J. P. Teixeira, J. M. V Cunha, M. J. Mendes, S. Haque, J. Borme, H. Águas, E. Fortunato, R. Martins, J. C. González, J. P. Leitão, P. A. Fernandes, M. Edoff and S. Sadewasser, *Adv. Mater. Interfaces*, 2018, **5**, 1701101.

7 D. Ledinek, P. Salome, C. Hagglund, U. Zimmermann and M. Edoff, *IEEE J. Photovoltaics*, 2018, **8**, 864.

8 B. Vermang, V. Fjällström, J. Pettersson, P. Salomé and M. Edoff, *Sol. Energy Mater. Sol. Cells*, 2013, **117**, 505–511.

9 B. Vermang, J. T. Wätjen, V. Fjällström, F. Rostvall, M. Edoff, R. Kotipalli, F. Henry and D. Flandre, *Prog. Photovoltaics Res. Appl.*, 2014, **22**, 1023.

10 S. Bose, J. M. V. Cunha, J. P. Teixeira, J. P. Leitão, J. Borme, J. Gaspar, P. A. Fernandes, M. Edoff and P. M. P. Salomé, *Submitt. to Thin Solid Film.*

11 J. Zhao, A. Wang and M. A. Green, in *IEEE Conference on Photovoltaic Specialists*, IEEE, 1990, pp. 333–335.

12 E. Schneiderlöchner, R. Preu, R. Lüdemann and S. W. Glunz, *Prog. Photovoltaics Res. Appl.*, 2002, **10**, 29.

13 T. Dullweber, S. Gatz, H. Hannebauer, T. Falcon, R. Hesse, J. Schmidt and R. Brendel, *Prog. Photovoltaics Res. Appl.*, 2012, **20**, 630.

14 M. Moors, K. Baert, T. Caremans, F. Duerinckx, A. Cacciato and J. Szlufcik, *Sol. Energy Mater. Sol. Cells*, 2012, **106**, 84.

15 P. Casper, R. Hünig, G. Gomard, O. Kiowski, C. Reitz, U. Lemmer, M. Powalla and M. Hetterich, *Phys. Status Solidi - Rapid Res. Lett.*, 2016, **10**, 376–380.

16 J. M. V. Cunha, P. A. Fernandes, A. Hultqvist, J. P. Teixeira, S. Bose, B. Vermang, S. Garud, D. Buldu, J. Gaspar, M. Edoff, J. P. Leitao and P. M. P. Salome, *IEEE J. Photovoltaics*, 2018, 1.

17 C. van Lare, G. Yin, A. Polman and M. Schmid, *ACS Nano*, 2015, **9**, 9603.

18 G. Yin, M. Song, S. Duan, P. Manley, D. Greiner, C. A. Kaufmann and M. Schmid, *ACS Appl. Mater. Interfaces*, 2016, **8**, 31646.

19 G. Yin, P. Manley and M. Schmid, *Sol. Energy*, 2018, **163**, 443.

20 G. Yin, P. Manley and M. Schmid, *Sol. Energy Mater. Sol. Cells*, 2016, **153**, 124.

21 G. Yin, M. W. Knight, M.-C. van Lare, M. M. Solà Garcia, A. Polman and M. Schmid, *Adv. Opt. Mater.*, 2017, **5**, 1600637.

22 S. Garud, N. Gampa, T. G. Allen, R. Kotipalli, D. Flandre, M. Batuk, J. Hadermann, M. Meuris, J. Poortmans, A. Smets and B. Vermang, *Phys. status solidi*, 2018, **215**, 1700826.

23 B. Vermang, Y. Ren, O. Donzel-Gargand, C. Frisk, J. Joel, P. Salome, J. Borme, S. Sadewasser, C. Platzer-Bjorkman and M. Edoff, *IEEE J. Photovoltaics*, 2016, **6**, 332–336.

24 S. Garud, B. Vermang, S. Sahayaraj, S. Ranjbar, G. Brammertz, M. Meuris, A. Smets and J. Poortmans, in *Physica Status Solidi (C) Current Topics in Solid State Physics*, 2017, vol. 14, pp. 2–7.

25 P. M. P. Salomé, V. Fjallstrom, A. Hultqvist, P. Szaniawski, U. Zimmermann and M. Edoff, *Prog. Photovoltaics Res. Appl.*, 2013, **22**, 83.

26 J. H. Werner, J. Mattheis and U. Rau, *Thin Solid Films*, 2005, **480**–**481**, 399.

27 M. Schmid, J. Klaer, R. Klenk, M. Topič and J. Krč, *Thin Solid Films*, 2013, **527**, 308.

28 G. Yin, V. Brackmann, V. Hoffmann and M. Schmid, *Sol. Energy Mater. Sol. Cells*, 2015, **132**, 142.

29 M. Schmid, *Semicond. Sci. Technol.*, 2017, **32**, 043003.

30 G. Yin, A. Steigert, P. Andrae, M. Goebelt, M. Latzel, P. Manley, I. Lauermann, S. Christiansen and M. Schmid, *Appl. Surf. Sci.*, 2015, **355**, 800.

31 A. S. Sokolov, S. K. Son, D. Lim, H. H. Han, Y.-R. Jeon, J. H. Lee and C. Choi, *J. Am. Ceram. Soc.*, 2017, **100**, 5638.